

# On discrete symmetries of robotics systems: A group-theoretic and data-driven analysis

Daniel Ordonez-Aprahez\*, Mario Martin<sup>†‡</sup>, Antonio Agudo\* and Francesc Moreno-Noguer\*

\* Institut de Robòtica i Informàtica Industrial, CSIC-UPC. <sup>†</sup>Barcelona Supercomputing Center (BSC).

<sup>‡</sup> Departament de Ciències de la Computació, Universitat Politècnica de Catalunya (UPC).

[dordonez, aagudo, fmoreno]@iri.upc.edu, mmartin@cs.upc.edu

**Abstract**—In this work, we study discrete morphological symmetries of dynamical systems, a predominant feature in animal biology and robotic systems, expressed when the system’s morphology has one or more planes of symmetry describing the duplication and balanced distribution of body parts. These morphological symmetries imply that the system’s dynamics are symmetric (or approximately symmetric), which in turn imprints symmetries in optimal control policies and in all proprioceptive and exteroceptive measurements related to the evolution of the system’s dynamics. For data-driven methods, symmetry represents an inductive bias that justifies data augmentation and the construction of symmetric function approximators. To this end, we use group theory to present a theoretical and practical framework allowing for (1) the identification of the system’s morphological symmetry group  $\mathcal{G}$ , (2) data-augmentation of proprioceptive and exteroceptive measurements, and (3) the exploitation of data symmetries through the use of  $\mathcal{G}$ -equivariant/invariant neural networks, for which we present experimental results on synthetic and real-world applications, demonstrating how symmetry constraints lead to better sample efficiency and generalization while reducing the number of trainable parameters.

## I. INTRODUCTION

Discrete Morphological Symmetries (DMS) are a predominant feature in biology. The vast majority of living and extinct animal species (including humans) feature bilateral/sagittal reflection symmetry (i.e., the right side of the body is approximately a reflection of the left one. See fig. 1-left). While a significant number of species feature radial symmetry (i.e., two or more morphological symmetry planes. See fig. 1-center) [12]. Likewise, most robotic systems share these symmetries due to bio-mimicry design and the precise duplication of body parts and mechanisms.

In biology, morphological symmetries are related to the duplication and balanced distribution of body parts [12]. However, in order to study these phenomena in dynamical systems theory, we present a more rigorous definition (section IV), which, loosely speaking, defines a DMS as an energy-preserving linear-transformation of the system state configuration allowing it to *imitate* a Euclidean isometry (i.e., a reflection/rotation + translation of space). For instance, see how the bipedal robot Atlas and the quadruped Solo in fig. 1 *imitate* the reflection of space ( $g_s$ ) with a discrete change in their body and limbs pose (i.e., their state configuration).

These morphological symmetries imply that the dynamics and control of body motions are symmetric [29], which in turn,

imprints symmetries in all proprioceptive and exteroceptive measurements related to the evolution of the system’s dynamics (e.g. joint torques, depth images, contact forces). Therefore, for systems with morphological symmetries, we can use data augmentation to mitigate the challenges of data collection in robotics, computer graphics, and computational biology. Additionally, in data-driven applications, we can impose symmetry constraints in machine learning algorithms to boost sample efficiency and enhance generalization [29, 7, 23].

Despite the potential benefits of exploiting symmetry and the ubiquitous presence of morphological symmetries in robotic systems, animals, and animated characters; this relevant inductive bias is frequently left unexploited in data-driven applications in the fields of robotics, computer graphics, and computational biology. We attribute the scarce adoption of these techniques to (1) a missing theoretical framework that consolidates the concept of morphological symmetries, facilitating their study and *identification*, and (2) a missing practical framework enabling the *efficient and convenient* exploitation of symmetries in real-world data-driven applications.

The absence of a clear theoretical framework makes the process of identifying morphological symmetries (and the symmetries of proprioceptive and exteroceptive data) a laborious system-specific and error-prone process. Thus, it is of no surprise that most recent works exploiting some morphological symmetry (see [27, 1, 28] in computer graphics, and [23, 16, 10, 6] in robotics/dynamical systems) have done so only for simple systems and for the simplest morphological symmetry: the reflection/sagittal symmetry (see fig. 1-left) (with exception of Finzi et al. [6]). While giving no insights on how to apply these techniques to other systems (especially to systems with more than a single morphological symmetry).

Contrary to previous works, the focus of this paper is on understanding morphological symmetries and presenting the theoretical abstractions that allow studying these phenomena in *arbitrary* dynamical systems with *any* number of symmetries. To achieve this, we are required to study morphological symmetries from the lens of dynamical systems and of group theory (the field of mathematics that studies symmetries, broadly used in physics and machine learning) (sections II and III). In summary, our work presents the following *theoretical* contributions: nosep, leftmargin=2em

✱ A definition of the set of DMSs of a dynamical system as a *symmetry group*  $\mathcal{G}$ , isomorphic to a group of isometries

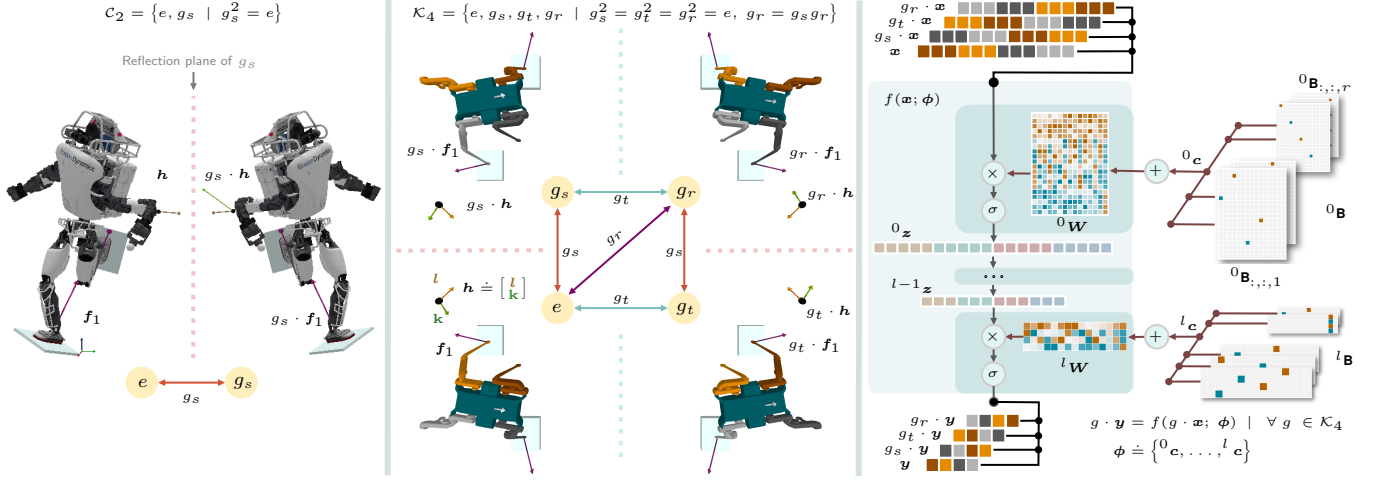


Fig. 1: **Left:** Symmetric configurations of the bipedal robot Atlas (3D animation), whose morphological symmetry (described by the reflection group  $C_2$ ) allow it to imitate the reflections of space  $g_s$  (hint: see how the text on the robot’s chest is not reflected). **Middle:** Top-view of symmetric configurations of the quadruped robot Solo (3D animation), whose morphological symmetries (described by the Klein four-group  $K_4$ ) allow it to imitate two perpendicular reflections ( $g_s, g_t$ ) and a  $180^\circ$  rotation ( $g_r$ ) of space (hint: see how the robot’s heading direction and legs coloring are not reflected/rotated). Symmetry transformations (arrows) affect the robot configuration, along with proprioceptive (center of mass linear  $l$  and angular  $k$  momentum) and exteroceptive measurements (terrain elevation, external force  $f_1$ ). **Right:** diagram of a toy  $K_4$ -equivariant neural network, processing the symmetric states of robot Solo  $x$  and outputting the symmetric binary feet contact states  $y$  (see section V).

of the Euclidean space (section IV).

- ✱ A characterization of how DMSs translate to the symmetries of the system’s state and any proprioceptive and exteroceptive measurements. Facilitating the identification of  $\mathcal{G}$  and the use of data augmentation (section IV-A).

Lastly, our **practical** contributions (section V) are: nosep, leftmargin=2em

- ❖ An open-access repository<sup>1</sup> enabling the prototyping of  $\mathcal{G}$ -equivariant Neural Networks (NN) for arbitrary DMS.
- ❖ Mitigation of the computational and memory complexity of equivariant architectures. Enabling the construction of large-scale  $\mathcal{G}$ -equivariant NN.
- ❖ We show an approximate  $1/|\mathcal{G}|$  reduction in the trainable parameters of NN. Being  $|\mathcal{G}|$  the number of DMSs.
- ❖ We derived an optimal initialization for the trainable parameters of  $\mathcal{G}$ -equivariant NN layers.

Lastly, we provide optional appendices where we extend our theoretical derivations and provide tutorial-like examples.

## II. BACKGROUND ON SYMMETRY GROUPS

Group theory is the default language for studying symmetry transformations. Thus, we provide a shallow introduction to the field<sup>2</sup> and define the notation required for our development. In a nutshell, a symmetry group in group theory is an abstraction of the **set** of symmetries that **different** geometric objects have. Understanding symmetry as a **transformation** that conserves a relevant property of the object (e.g. energy).

<sup>1</sup> [github.com/Danfoa/RobotEquivariantNN](https://github.com/Danfoa/RobotEquivariantNN)

<sup>2</sup>Being this short section undoubtedly an unsatisfactory introduction to group theory, we refer the uninitiated and interested reader to Carter [5] for intuition and to Bronstein et al. [3] for a machine learning introduction.

For instance, in fig. 1-left the reflection group  $C_2$  describes the symmetries that vectors, pseudo-vectors, rigid-bodies, and the robot atlas have to a reflection of space  $g_s$ . Being the symmetries, transformations preserving vector magnitudes and the energy of the robot. Similarly in fig. 1-center, the Klein four-group  $K_4$  describes the symmetries that the quadruped robot Solo has to  $180^\circ$  rotations ( $g_r$ ) and two perpendicular reflections ( $g_s, g_t$ ). While on fig. 1-right the same group describes the symmetries of the input  $x$  and output  $y$  vector spaces of a  $K_4$ -equivariant NN.

This flexible formalism allows us to study the set of morphological symmetries of a system as a symmetry group. Formally, a symmetry group is a set of invertible symmetry transformations (or **actions**)  $\mathcal{G} = \{e, g_1, g_1^{-1}, g_2, \dots\}$ , having an associative composition operator  $(\cdot) : \mathcal{G} \times \mathcal{G} \rightarrow \mathcal{G}$  mapping group actions to other group actions. And containing the trivial action  $e$  (leaving objects unchanged). Not surprisingly, a group action acts differently on different objects. Here, is where group **representations** allow us to use the familiar language of linear algebra to characterize how an action  $g$  transforms a specific geometric object, say  $x \in \mathcal{X} \subseteq \mathbb{R}^k$ . A representation  $\rho_{\mathcal{X}} : \mathcal{G} \rightarrow GL(k)$  is a mapping from group actions to the set of invertible square matrices of  $k$  dimensions (i.e., the General Linear group  $GL$ ). Thus, a representation specifies how objects  $x \in \mathcal{X}$  are transformed by group actions:  $g \cdot x \doteq \rho_{\mathcal{X}}(g)x$ .

A fundamental concept for this work is the notion of function  $\mathcal{G}$ -equivariance and  $\mathcal{G}$ -invariance. The function  $f : \mathbb{R}^n \rightarrow \mathbb{R}^m$ , is said to be  $\mathcal{G}$ -equivariant or  $\mathcal{G}$ -invariant if:

$$\underbrace{g \cdot y = f(g \cdot x)}_{\text{Equivariance}} \mid \forall g \in \mathcal{G} \quad \text{or} \quad \underbrace{y = f(g \cdot x)}_{\text{Invariance}} \mid \forall g \in \mathcal{G}. \quad (1)$$

Roughly speaking, an equivariant function maps symmetries

of the input to symmetries of the output, while an invariant function maps symmetries of the input to an invariant output.

### III. LAGRANGIAN MECHANICS AND SYMMETRIES OF DYNAMICAL SYSTEMS

Here we provide a group-theoretic perspective of symmetries in an arbitrary dynamical system. The definitions and notations of this section are fundamental for understanding the objective of this work, namely DMSs. To this end, let us consider a dynamical system with generalized coordinates  $\mathbf{q} \in \mathcal{Q} \subseteq \mathbb{R}^n$  and velocities  $\dot{\mathbf{q}} \in \mathcal{T}_{\mathbf{q}}\mathcal{Q} \subseteq \mathbb{R}^n$ . Being  $\mathcal{Q}$  the constrained configuration space, and  $\mathcal{T}_{\mathbf{q}}\mathcal{Q}$  the space of constrained generalized velocities (i.e., the configuration tangent space at  $\mathbf{q}$ ). Additionally, consider a Lagrangian function  $\mathcal{L} : \mathcal{Q} \times \mathcal{T}_{\mathbf{q}}\mathcal{Q} \rightarrow \mathbb{R} = \mathcal{T}(\mathbf{q}, \dot{\mathbf{q}}) - \mathcal{U}(\mathbf{q}, \dot{\mathbf{q}})$  specifying the total energy of the system at any state. Where  $\mathcal{T}(\mathbf{q}, \dot{\mathbf{q}})$ ,  $\mathcal{U}(\mathbf{q}, \dot{\mathbf{q}})$  describe the state kinetic and potential energies, respectively.

The symmetries of a dynamical system are defined as transformations in the space of generalized coordinates that keep the total energy of the system invariant [18, 14]. In this work, we study time-invariant linear transformations of generalized coordinates  $\rho_{\mathcal{Q}}(g) : \mathbb{R}^n \rightarrow \mathbb{R}^n$ , which are interpreted as the representations of actions of a symmetry group:  $g \cdot \mathbf{q} \doteq \rho_{\mathcal{Q}}(g)\mathbf{q} \mid \forall \mathbf{q} \in \mathcal{Q}, g \in \mathcal{G}$ . Note that because of the linearity of the transformation, the velocity and acceleration of the transformed coordinates are given by  $g \cdot \dot{\mathbf{q}} \doteq \rho_{\mathcal{Q}}(g)\dot{\mathbf{q}}$  and  $g \cdot \ddot{\mathbf{q}} \doteq \rho_{\mathcal{Q}}(g)\ddot{\mathbf{q}}$ , respectively.

Formally, we say that a dynamical system has a symmetry group  $\mathcal{G}$  if its **Lagrangian is  $\mathcal{G}$ -invariant**:

$$\mathcal{L}(\mathbf{q}, \dot{\mathbf{q}}) = \mathcal{L}(g \cdot \mathbf{q}, g \cdot \dot{\mathbf{q}}) \mid \forall g \in \mathcal{G}, \mathbf{q} \in \mathcal{Q}, \dot{\mathbf{q}} \in \mathcal{T}_{\mathbf{q}}\mathcal{Q}. \quad (2)$$

Being  $g$  a **feasible** symmetry if the transformed state is a feasible state, i.e. when  $g \cdot \mathbf{q} \in \mathcal{Q}$  and  $g \cdot \dot{\mathbf{q}} \in \mathcal{T}_{\mathbf{q}}\mathcal{Q}$  (assuming both  $\mathcal{Q}$  and  $\mathcal{T}_{\mathbf{q}}\mathcal{Q}$  are connected sets).

Since the Lagrangian structure differs between the original  $(\mathbf{q}, \dot{\mathbf{q}})$  and transformed coordinates  $(g \cdot \mathbf{q}, g \cdot \dot{\mathbf{q}}) \mid \forall g \in \mathcal{G}$ , when we derive the Equations of Motion (EoM) of the system in the set of transformed coordinates, we obtain a set of EoMs describing the true system dynamics in different coordinate systems. Formally, if we derive the EoM through the Euler-Lagrange equation of the second order  $(\frac{d}{dt} \frac{\partial \mathcal{L}(\mathbf{q}, \dot{\mathbf{q}})}{\partial \dot{\mathbf{q}}} - \frac{\partial \mathcal{L}(\mathbf{q}, \dot{\mathbf{q}})}{\partial \mathbf{q}} \equiv \mathbf{M}(\mathbf{q})\ddot{\mathbf{q}} - \boldsymbol{\tau}(\mathbf{q}, \dot{\mathbf{q}}) = \mathbf{0})$ , the distinct EoM are equivariant to each other [14], a property we will refer to as **dynamics  $\mathcal{G}$ -equivariance**:

$$\underbrace{g \cdot [\mathbf{M}(\mathbf{q})\ddot{\mathbf{q}}]}_{\text{Inertial}} - \underbrace{\boldsymbol{\tau}(\mathbf{q}, \dot{\mathbf{q}})}_{\text{Moving}} = \underbrace{\mathbf{M}(g \cdot \mathbf{q})g \cdot \ddot{\mathbf{q}}}_{\text{Inertial}} - \underbrace{\boldsymbol{\tau}(g \cdot \mathbf{q}, g \cdot \dot{\mathbf{q}})}_{\text{Moving}} = \mathbf{0} \mid \forall g \in \mathcal{G}, \mathbf{q} \in \mathcal{Q}, \dot{\mathbf{q}} \in \mathcal{T}_{\mathbf{q}}\mathcal{Q}. \quad (3)$$

Denoting  $\mathbf{M}(\mathbf{q}) : \mathcal{Q} \rightarrow \mathbb{R}^{n \times n}$  as the generalized mass matrix function and  $\boldsymbol{\tau}(\mathbf{q}, \dot{\mathbf{q}}) : \mathcal{Q} \times \mathcal{T}_{\mathbf{q}}\mathcal{Q} \rightarrow \mathbb{R}^n$  as the generalized moving forces at a given state  $(\mathbf{q}, \dot{\mathbf{q}})$ . Note that, in eq. (3) the original and transformed dynamics are related linearly by the Jacobian of the coordinate transformation [25]. Which in this case is  $\rho_{\mathcal{Q}}(g)$  (reduced to  $g$  to preserve notation).

Note that to ensure dynamics  $\mathcal{G}$ -equivariance (eq. (3)), both the generalized inertial and moving forces need to be independently equivariant, implying:

$$\mathbf{M}(g \cdot \mathbf{q}) = g\mathbf{M}(\mathbf{q})g^{-1} \quad \wedge \quad g \cdot \boldsymbol{\tau}(\mathbf{q}, \dot{\mathbf{q}}) = \boldsymbol{\tau}(g \cdot \mathbf{q}, g \cdot \dot{\mathbf{q}}) \mid \forall g \in \mathcal{G}, \mathbf{q} \in \mathcal{Q}, \dot{\mathbf{q}} \in \mathcal{T}_{\mathbf{q}}\mathcal{Q}. \quad (4)$$

The resultant  $\mathcal{G}$ -equivariance of the generalized mass matrix becomes an identifying property of symmetrical systems, providing a pathway for the **identification** of action representations of the symmetry group  $\rho_{\mathcal{Q}}(g) \mid g \in \mathcal{G}$  (section IV-B). While the equivariance of the generalized moving forces (which in practice usually incorporates control, constraint, and external forces) implies that dynamics  $\mathcal{G}$ -equivariance (eq. (3)) is upheld until a **symmetry breaking force** violates the equivariance of  $\boldsymbol{\tau}$ .

To gain some intuition, consider the bipedal robot Atlas with a symmetry group  $\mathcal{G} = \mathcal{C}_2 = \{e, g_s\}$ . For this system, eq. (2) says that both robot states in fig. 1-left are symmetric states (related by the action  $g_s$ ). Then, eq. (3) says that any motion trajectory of the robot to the left is equivalent (up to transformation by  $g_s$ ) to the motion trajectory of the robot to the right. This, if both motion trajectories feature  $\mathcal{C}_2$ -equivariant control and external interactions (eq. (4)). A similar analysis follows for systems with larger symmetry groups (e.g. Solo in fig. 1-center).

#### A. Floating-base dynamical systems

Let us now narrow our focus to floating-base dynamical systems. Namely, legged/flying/swimming/moving robots, animals, and animated characters evolving in a Euclidean space of  $d$  dimensions (space embedded with its corresponding Euclidean group of isometries  $\mathbb{E}_d$ , representing  $d$ -dimensional rotations/reflections + translations), being  $d \in \{0, 1, 2, 3\}$ . For these systems, the generalized coordinates can be decoupled into  $\mathbf{q} = \begin{bmatrix} \mathbf{X}_B \\ \hat{\mathbf{q}} \end{bmatrix} \in \mathcal{Q} \doteq \mathbb{E}_d \times \mathcal{Q}_J$ . Where  $\mathbf{X}_B \in \mathbb{E}_d$  represents the system's base (or center of mass (CoM)) position and orientation<sup>3</sup>,  $\hat{\mathbf{q}} \in \mathcal{Q}_J \subseteq \mathbb{R}^{n_J}$  represents the internal Degrees of Freedom (DoF) configuration, and  $\mathcal{Q}_J$  is the internal constrained configuration space, commonly referred to as joint-space. In this coordinate space, we can decouple the effect of the symmetry actions  $g$  on  $\mathbb{E}_d$  and  $\mathcal{Q}_J$ , noting that:  $g \cdot \mathbf{q} = \rho_{\mathcal{Q}}(g) \mathbf{q} = \begin{bmatrix} \rho_{\mathbb{E}_d}(g) & \mathbf{0} \\ \mathbf{0} & \rho_{\mathcal{Q}_J}(g) \end{bmatrix} \begin{bmatrix} \mathbf{X}_B \\ \hat{\mathbf{q}} \end{bmatrix} \mid \forall g \in \mathcal{G}$ . With representation  $\rho_{\mathbb{E}_d}(g) \in \mathbb{E}_d$  being a homogeneous matrix transformation affecting the base, and  $\rho_{\mathcal{Q}_J}(g) \in \mathbb{R}^{n_J \times n_J}$  describing the transformation of the joint-space configuration. This decoupling enables the differentiation between the system's morphological symmetries (section IV) and symmetries to Euclidean isometries.

**Symmetries to Euclidean isometries:** floating-base systems are known for having symmetries to (some) continuous translations and/or rotations/reflections of space. These symmetries belong to a subset of the Euclidean group  $\bar{g} \in \mathbb{E}_d$  (denoted

<sup>3</sup>We deliberately abuse notation to keep the homogeneous matrix representation  $\mathbf{X}_B$  of position and orientation, instead of the vector-quaternion representation, common in robotics and computer graphics.

as  $\bar{g}$  to highlight that the action represents a true Euclidean isometry). The identifying property of these symmetries is the invariance of the system's joint-space  $\rho_{Q_J}(\bar{g}) = \mathbf{I}_{n_J} \mid \forall \bar{g} \in \mathbb{E}_d$ , contrary to DMSs (section IV). For instance, the robot Atlas (fig. 1) is symmetric to true reflections of space and to horizontal translations (eq. (2)). These transformations leave the joint-space configuration invariant, while the dynamics of the transformed system is related to the original up to the reflection/translation (eq. (3)).

#### IV. DISCRETE MORPHOLOGICAL SYMMETRIES (DMSs)

A DMS is a mathematical formalization of the property of some dynamical systems that can imitate the effect of rotations, translations, and infeasible reflections of space with a feasible discrete change in the system configuration. To understand DMSs it is helpful to first study the most simple (and most frequent) DMS: the reflection symmetry, which all humans and most animals approximately possess [12].

*Reflection DMS* ( $\mathcal{G} = \mathcal{C}_2$ ): Despite most floating-base dynamical systems being symmetric (eq. (2)) to **reflections** of space ( $\bar{g} \in \mathbb{E}_d$ ), in practice, it is common to ignore reflection symmetries, since, in general, it is infeasible to subject a real-world dynamical system to a true reflection of space [21]. However, systems with sagittal symmetry (e.g., Atlas in fig. 1-left, or the reader of this work) can **imitate** the effect of a true reflection of space with a feasible discrete change in the system's configuration (i.e., modifying your internal configuration (your body pose), and rotating and translating your base/hip). Therefore, Atlas and you share the same DMS, making your DMS group the reflection group  $\mathcal{G} = \mathcal{C}_2$ .

*Multiple DMSs* ( $|\mathcal{G}| > 2$ ): When a floating-base system has  $k \geq 2$  DMSs it is able to imitate more than a single Euclidean isometry (i.e., some subset of rotation/reflections + translations) (see fig. 1-center). For these systems, the set of DMSs forms a group  $\mathcal{G}$  that is isomorphic to a subset of Euclidean isometries (i.e., there is a one-to-one invertible mapping between the set  $g \in \mathcal{G}$  and a subset of  $|\mathcal{G}|$  Euclidean isometries  $\bar{g} \in \mathbb{E}_d$ ). Most frequently  $\mathcal{G}$  is a Cyclic  $\mathcal{C}_k$  group (for systems able to imitate  $k$  distinct rotations) or Dihedral  $\mathcal{D}_{2k}$  group (for systems able to imitate  $k$  distinct rotations and a reflection). See examples for  $\mathcal{C}_3$  in fig. 6, and for  $\mathcal{D}_4 \equiv \mathcal{K}_4$  in fig. 1-center. However, the symmetries in  $\mathcal{G}$  could imitate a finite or infinite set of Euclidean isometries.

**Definition** (Discrete morphological symmetry). A floating-base dynamical system with generalized coordinates  $\mathbf{q} \in \mathcal{Q} \doteq \mathbb{E}_d \times \mathcal{Q}_J$ , is said to have a DMS if, for a given Euclidean isometry  $\bar{g} \in \mathbb{E}_d$ , there exists an action  $g \in \mathcal{G}$ , with a **proper** representation in  $\mathbb{E}_d$  ( $|\rho_{\mathbb{E}_d}(g)| = 1$ ) and a **non-trivial** representation in joint-space ( $\rho_{Q_J}(g) \neq \mathbf{I}_{n_J}$ ), such that both  $g$  and  $\bar{g}$  are equivalent symmetries of the system:

$$\begin{aligned} \mathcal{L}(\mathbf{q}, \dot{\mathbf{q}}) &= \mathcal{L}(\bar{g} \cdot \mathbf{q}, \bar{g} \cdot \dot{\mathbf{q}}) = \mathcal{L}(g \cdot \mathbf{q}, g \cdot \dot{\mathbf{q}}) \\ |g \in \mathcal{G}, \bar{g} \in \mathbb{E}_d, \forall g \cdot \mathbf{q}, \mathbf{q} \in \mathcal{Q}, g \cdot \dot{\mathbf{q}}, \dot{\mathbf{q}} \in \mathbf{T}_q \mathcal{Q}. \end{aligned} \quad (5)$$

The set of DMSs of a dynamical system forms its symmetry group  $\mathcal{G}$ . The characteristic properties of these symmetries are

that they represent feasible transformations involving a change in joint-space configuration.

Having identified a potential Euclidean isometry to imitate  $\bar{g} \in \mathbb{E}_d$ , we can determine  $\rho_{\mathbb{E}_d}(g)$ . Since at any system state:

$$\begin{aligned} \mathcal{L}\left(\begin{bmatrix} \rho_{\mathbb{E}_d}(\bar{g})\mathbf{X}_B \\ \dot{\mathbf{q}} \end{bmatrix}, \begin{bmatrix} \rho_{\mathbb{E}_d}(\bar{g})\dot{\mathbf{X}}_B \\ \dot{\mathbf{q}} \end{bmatrix}\right) &= \mathcal{L}\left(\begin{bmatrix} \rho_{\mathbb{E}_d}(g)\mathbf{X}_B \\ \rho_{Q_J}(g)\dot{\mathbf{q}} \end{bmatrix}, \begin{bmatrix} \rho_{\mathbb{E}_d}(g)\dot{\mathbf{X}}_B \\ \rho_{Q_J}(g)\dot{\mathbf{q}} \end{bmatrix}\right) \\ &\quad \left| \begin{array}{l} |\rho_{\mathbb{E}_d}(\bar{g})| = \pm 1, |\rho_{\mathbb{E}_d}(g)| = 1 \\ \rho_{\mathbb{E}_d}(g)\mathbf{X} = \rho_{\mathbb{E}_d}(\bar{g})\mathbf{X}\rho_{\mathbb{E}_d}(\bar{g})^{-1} \end{array} \right. \quad (6) \end{aligned}$$

This structure of the proper transformation  $\rho_{\mathbb{E}_d}(g)\mathbf{X} = \rho_{\mathbb{E}_d}(\bar{g})\mathbf{X}\rho_{\mathbb{E}_d}(\bar{g})^{-1}$ , along with the  $\mathcal{G}$ -equivariant nature of the system generalized mass matrix (eq. (4)), provide a pathway for the identification of  $\mathcal{G}$  and the representations  $\rho_Q(g) \mid \forall g \in \mathcal{G}$  for any floating-base dynamical system (section IV-C).

#### A. Data augmentation in systems with DMS

Recall from section III that due to the linearity of the transformation  $g \cdot \mathbf{q} = \rho_Q(g)\mathbf{q}$ , the same action representation  $\rho_Q(g)$  acts on elements of the configuration tangent space  $\mathbf{T}_q \mathcal{Q}$  and any higher order tangent spaces:  $g \cdot \dot{\mathbf{q}} = \rho_Q(g)\dot{\mathbf{q}}$ ,  $g \cdot \ddot{\mathbf{q}} = \rho_Q(g)\ddot{\mathbf{q}}$ , including generalized forces  $g \cdot \boldsymbol{\tau} = \rho_Q(g)\boldsymbol{\tau}$  (eq. (3)). Since our floating-base systems' configuration space has the structure  $\mathcal{Q} \doteq \mathbb{E}_d \times \mathcal{Q}_J$ , this property translates to the action representations on  $\mathbb{E}_d$  and  $\mathcal{Q}_J$ . This effectively implies that  $\rho_{\mathbb{E}_d}(g)$  can be used to augment elements of  $\mathbb{E}_d$  and of  $\mathbb{E}_d$  higher order tangent spaces (i.e., points, vectors, pseudo-vectors, orientations, linear & angular velocities/accelerations). Likewise the representation  $\rho_{Q_J}(g)$  can be used to augment members of  $\mathcal{Q}_J$  and its higher order tangent spaces (i.e., joints positions/velocities/accelerations, joint forces/torques).

In practice, this means that any proprioceptive (e.g., joint torques, contact forces) and exteroceptive (e.g., point clouds, terrain height maps, RGBD-images) measurements relevant to the evolution of the system's dynamics, can be augmented solely with combinations of  $\rho_{\mathbb{E}_d}(\bar{g})$ ,  $\rho_{\mathbb{E}_d}(g)$  and  $\rho_{Q_J}(g)$ , as these measurements are composed of elements in  $\mathcal{Q}$  and  $\mathbb{E}_d$  and their higher order tangent spaces (see examples in sections C-C1 and C-D1). Furthermore, any data point will have  $|\mathcal{G}|$  symmetric data points, being  $|\mathcal{G}|$  the order of the group (i.e., the number of symmetries). This, roughly implies that for every minute of recorded data of a system with a symmetry group of order  $|\mathcal{G}| = 4$  (e.g. fig. 1-center) we can obtain an additional 3 minutes of recordings, solely by considering the symmetric states of the recorded data.

To exploit the measurements' symmetries we need to identify the joint-space representations  $\rho_{Q_J}(g)$ . However, this requires further assumptions over the nature of the system. Here, we study the case of rigid-body dynamics, but a similar analysis is possible for other types of systems, e.g., soft robots.

#### B. DMS in the case of rigid-body dynamics

In this section, we assume the system dynamics are ruled by rigid-body dynamics. Implying that our system is a collection of  $n_B$  interconnected rigid bodies. This is the usual scenario in robotics, computer graphics, and computational biology.



In rigid body dynamics, the generalized mass matrix is given by  $\mathbf{M}(\mathbf{q}) = \sum_k^{n_B} \mathbf{J}_{T_k}(\mathbf{q})^\top m_k \mathbf{J}_{T_k}(\mathbf{q}) + \mathbf{J}_{R_k}(\mathbf{q})^\top \mathbf{I}_k \mathbf{J}_{R_k}(\mathbf{q})$ , being  $\mathbf{J}_{T_k}(\mathbf{q}) : \mathbf{Q} \rightarrow \mathbb{R}^{d \times n}$  and  $\mathbf{J}_{R_k}(\mathbf{q}) : \mathbf{Q} \rightarrow \mathbb{R}^{d \times n}$  the position and orientation Jacobians, used to map generalized velocities to the linear ( $\dot{\mathbf{r}}_k = \mathbf{J}_{T_k}(\mathbf{q})\dot{\mathbf{q}}$ ) and angular ( $\mathbf{w}_k = \mathbf{J}_{R_k}(\mathbf{q})\dot{\mathbf{q}}$ ) velocities of the body  $k$  [26]. With  $\mathbf{M}(\mathbf{q})$ , we can formulate the kinetic energy of the system as  $\mathcal{T}(\mathbf{q}, \dot{\mathbf{q}}) = \frac{1}{2} \sum_k^{n_B} m_k \dot{\mathbf{r}}_k^2 + \mathbf{w}_k^\top \mathbf{I}_k \mathbf{w}_k = \frac{1}{2} \dot{\mathbf{q}}^\top \mathbf{M}(\mathbf{q}) \dot{\mathbf{q}}$ . Allowing us to understand the  $\mathcal{G}$ -equivariance nature of  $\mathbf{M}(\mathbf{q})$  (eq. (4)) as required property for actions  $g \in \mathcal{G}$  to conserve kinetic energy.

These Jacobians are functions of the **kinematic parameters** of the system<sup>4</sup>. While the mass and inertia of all bodies are the system's **dynamic parameters**. A DMS implies symmetries over both kinematic and dynamic parameters.

*Symmetries of kinematic parameters (Kinematic Tree):* Roughly speaking, the symmetry in kinematic parameters can be interpreted as a kinematic tree symmetry. Requiring the DMS  $g$  to modify the system state such that the resultant kinematic tree is indistinguishable from the one obtained by applying the Euclidean isometry  $\bar{g}$ .

To see this, we ignore momentarily the dynamic parameters and study the  $\mathcal{G}$ -equivariant nature of  $\mathbf{M}(\mathbf{q})$  (eq. (4)). For any symmetry (eq. (2)) the rigid-body system must have positional and rotational Jacobians that respect  $\mathbf{J}_{T_i}(g \cdot \mathbf{q}) = \mathbf{J}_{T_k}(\mathbf{q})g^{-1} \wedge \mathbf{J}_{R_i}(g \cdot \mathbf{q}) = \mathbf{J}_{R_k}(\mathbf{q})g^{-1} \mid \forall g \in \mathcal{G}$ . If  $\mathcal{G}$  is a group of DMSs (i.e., each  $g \in \mathcal{G}$  imitates an Euclidean isometry  $\bar{g} \in \mathbb{E}_d$ ), we have that the  $i^{\text{th}}$  body Jacobians respect:

$$\begin{aligned} \mathbf{J}_{T_i}(g \cdot \mathbf{q})g &= \mathbf{J}_{T_k}(\bar{g} \cdot \mathbf{q}) = \mathbf{J}_{T_k}(\mathbf{q})\bar{g}^{-1} \quad \text{and} \\ \mathbf{J}_{R_i}(g \cdot \mathbf{q})g &= \mathbf{J}_{R_k}(\bar{g} \cdot \mathbf{q}) = \mathbf{J}_{R_k}(\mathbf{q})\bar{g}^{-1} \quad (7) \\ &\mid \forall \{(g, \bar{g}) \mid g \in \mathcal{G}, \bar{g} \in \mathbb{E}_d\}, \end{aligned}$$

where  $i$  is the body index in the kinematic tree result of applying action  $g$ , while  $k$  is the body index in the kinematic tree result of applying the Euclidean isometry  $\bar{g}$ . When  $k \neq i$  the representation  $\rho_{Q_J}(g)$  of the DMS, involves a permutation/exchange of body's  $i$  and  $k$  joint-space configuration. For instance, the action  $g_s$  exchanges the left and right legs configurations of robots Atlas and Solo in fig. 1.

However, kinematic tree symmetries (eq. (7)) is a required but not sufficient condition for DMSs. Additional symmetries over the dynamic parameters are required.

*Symmetries of dynamic parameters (Mass & Inertia):* Roughly speaking, in addition to the kinematic tree symmetry of eq. (7) (relating the configuration of bodies  $i$  and  $k$  in space) the mass, CoM, and the inertia of the bodies  $i$  and  $k$  need to be equivalent. This ensures the  $\mathcal{G}$ -equivariance of  $\mathbf{M}(\mathbf{q})$  (eq. (4)) and in turn the existence of the DMS (eq. (5)).

To understand this morphological constraint, consider the base body configuration  $\mathbf{X}_B \in \mathbb{E}_d$  transformed by the DMS ( $\rho_{\mathbb{E}_d}(g)\mathbf{X}_B = \rho_{\mathbb{E}_d}(\bar{g})\mathbf{X}_B\rho_{\mathbb{E}_d}(\bar{g})^{-1}$ )<sup>5</sup>, and transformed by the Euclidean isometry  $\bar{g}$ , which the DMS imitates, ( $\rho_{\mathbb{E}_d}(\bar{g})\mathbf{X}_B$ ).

<sup>4</sup>The Denavit–Hartenberg parameters are a common convention of kinematic parameters adopted in robotics and computer graphics.

<sup>5</sup>Where the action on the left of  $\mathbf{X}_B$  is interpreted as a Euclidean isometry of the base in a global reference frame and the action to the right as a Euclidean isometry in the frame attached to the base.

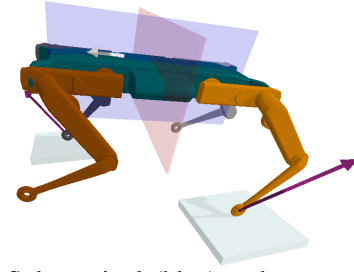


Fig. 2: Robot Solo sagittal (blue) and transversal (red) symmetry planes of the base rigid body.

For both base configurations to have the same dynamics, their CoM must coincide, and more importantly, the Inertia matrix  $\mathbf{I}_B$  in both configurations should be identical. Because in general,  $\rho_{\mathbb{E}_d}(g) \neq \rho_{\mathbb{E}_d}(\bar{g})$ , the rigid-body Inertia must be invariant to the right transformation  $\mathbf{X}_B\rho_{\mathbb{E}_d}(\bar{g})^{-1}$  (eq. (6)). This inertia invariance implies a **symmetric mass distribution** of the rigid body (see geometric proof in section A-B)).

To gain some intuition, consider the non-trivial example of robot Solo in fig. 1-center. This robot is able to imitate two reflections of space ( $\bar{g}_t, \bar{g}_s$ ) and a 180° rotation of space  $\bar{g}_r$ , because its base body has two symmetry planes (see fig. 2), making the reflected inertia of the base, at any arbitrary configuration, invariant under the transformation  $\mathbf{X}_B\rho_{\mathbb{E}_d}(\bar{g})^{-1} \mid \bar{g} \in \{e, \bar{g}_t, \bar{g}_s, \bar{g}_r\} \in \mathcal{K}_4$ . As discussed in section IV-C, the set of potential isometries that a DMS could imitate is the set of isometries to which the inertia of the base of the system is invariant.

Note, however, that we do not impose this inertia invariance constraint on other rigid bodies of the robot (the bodies composing each of the four legs). This happens when the kinematic tree is **modular** (i.e., has multiple kinematic subchains containing rigid bodies that are reflected or identical versions of rigid bodies in another subchain). For the robot Solo, this modularity is expressed in the left legs' rigid bodies being true reflections ( $g_s$ ) of the right legs' rigid bodies. While the front legs' bodies are true reflections ( $g_t$ ) of the hind legs' bodies.<sup>6</sup> This allows to determine  $\rho_{Q_J}(g) \mid \forall g \in \mathcal{K}_4$  as the exchange of configuration of left-right legs (for  $g_s$ ) and of front-hind legs (for  $g_t$ ). Complying with eq. (5) for all isometries.

### C. Identification of DMS group $\mathcal{G}$ in rigid-body dynamics

The identification of the DMS group  $\mathcal{G}$  of a floating-base dynamical system, composed of rigid-bodies, can be outlined in four steps (see tutorial examples in fig. 6):

- 1) Identify all the unique bodies of the kinematic tree (i.e., no duplicated or reflected version of the body in the tree) including the base of the system.
- 2) Identify the set of Euclidean isometries  $\bar{g} \in \mathbb{E}_d$  for which the inertia of each unique body is simultaneously invariant. These are the candidate Euclidean isometries for which DMSs of the system could exist.

<sup>6</sup>This front-hind reflection symmetry of the base and rigid bodies of the legs of the robot Solo is why this quadruped has additional DMSs ( $g_t$ ) compared to quadrupeds in nature.

- 3) Identify modularity in the kinematic tree. i.e., all sets of duplicated/reflected symmetric kinematic subchains.
- 4) From base to end-effectors use eq. (7) to determine for each  $\bar{g}$ , if the action  $g$  exists and its a feasible symmetry.

Although the analysis presented might appear to be excessive for simple systems and simple DMS groups, the abstractions presented open the door for the study of more complex systems and symmetry groups, for computational design of symmetric robotic systems, and for algorithmic identification of DMSs and data augmentation.

## V. $\mathcal{G}$ -EQUIVARIANT AND $\mathcal{G}$ -INVARIANT FUNCTION APPROXIMATORS

Once we identified the DMS group  $\mathcal{G}$  of our system, we know that any proprioceptive or exteroceptive measurements have the same symmetry group  $\mathcal{G}$  (section IV-A). Therefore, to improve generalization and sample efficiency, we can exploit the known symmetries of the input  $\mathbf{x}$  and output  $\mathbf{y}$  spaces, of any mapping we desire to approximate, by constructing  $\mathcal{G}$ -equivariant or  $\mathcal{G}$ -invariant (eq. (1)) NN  $f(\mathbf{x}; \phi)$ , with parameters  $\phi$  [2]. This section is built on top of Finzi et al. [7] framework for  $\mathcal{G}$ -equivariant NN. Our main motivation is to address the limitations that prohibit the construction of large-scale  $\mathcal{G}$ -equivariant NN, which are ubiquitous in real-life applications (see details in section B).

Consider  $f(\mathbf{x}; \phi)$  to be composed of multiple perceptrons (or convolutional) layers of the form  ${}^l\mathbf{y} := \sigma({}^l\mathbf{W}^l\mathbf{x} + {}^l\mathbf{b})$ , where  ${}^l\mathbf{x} \in \mathbb{R}^n$ ,  ${}^l\mathbf{y} \in \mathbb{R}^m$  are the  $l^{th}$  layer input-output.  ${}^l\mathbf{W} \in \mathbb{R}^{m \times n}$  and  ${}^l\mathbf{b}$  are the layer's linear map and bias; and  $\sigma : \mathbb{R} \rightarrow \mathbb{R}$  is a strictly monotonic nonlinearity [20]. With this parametrization, the equivariance constraints of eq. (1) can be reduced to constraints on the linear map  $\mathbf{W}$  (dropping the layer index  $l$  for notation clarity):<sup>7</sup>

$$\rho_{out}(g)\mathbf{W} = \mathbf{W}\rho_{in}(g) \iff (\rho_{\mathbf{W}}(g) - \mathbf{I})\mathbf{w} = \mathbf{0} \quad |\forall g \in \mathcal{G}. \quad (8)$$

The right-side of eq. (8) is a reformulation of the linear map equivariance constraints (left-side) as a standard set of linear equations. Denoting  $\mathbf{w} = \text{vec}(\mathbf{W}) \in \mathbb{R}^{mn}$  as a vectorized version of  $\mathbf{W}$  and  $\rho_{\mathbf{W}}(g) = \rho_{out}(g) \otimes \rho_{in}(g^{-1})^T \in \mathbb{R}^{mn \times mn}$  ( $\otimes$  stands for the Kronecker product) as the action representation acting on the parameter space of the linear map. Here, we consider the group acting on  $\mathbf{W}$  a *semi-direct product*<sup>8</sup> of the input and output groups (refer to Finzi et al. [7] for details). Since the constraint imposed by each  $g$  is linear in  $\mathbf{W}$ , we can stack them into a single large system of linear equations  $\mathbf{C}\mathbf{w} = \mathbf{0}$ . The nullspace of this system of equations  $\mathbf{B} \in \mathbb{R}^{mn \times r}$  describes the  $r$  basis vectors spawning the entire space of equivariant linear maps. Allowing to parameterize all  $\mathcal{G}$ -

equivariant  $\mathbf{W}$  as:

$$\mathbf{w} = \sum_k^r c_k \mathbf{B}_{:,k} \iff \mathbf{W} = \sum_k^r c_k \text{unvec}(\mathbf{B}_{:,k}) \quad (9) \\ \doteq \sum_k^r c_k \mathbf{B}_{:,k}$$

Where the basis coefficients  $\mathbf{c} \in \mathbb{R}^r$  represent the free variables of the system of equations and the *trainable parameters of the equivariant layer* (see fig. 1 right).

### A. Dealing with memory complexity of equivariant layers:

An equivariant layer needs to store the matrices  $\rho_{\mathbf{W}}(g) \in \mathbb{R}^{mn \times mn}$  and  $\mathbf{B} \in \mathbb{R}^{mn \times r}$ , in addition to the typical memory complexity of a perceptron or convolutional layer. These matrices' memory complexity quickly becomes intractable for moderate input-output dimensions (see section C). Fortunately, the symmetry groups of DMSs (finite groups) have sparse action matrix representations, resulting in both of the aforementioned matrices being sparse. Our implementation<sup>1</sup> extends the Pytorch API from Finzi et al. [7] to process finite groups with sparse matrix definitions limiting the additional memory footprint of equivariant layers to a minimum.

### B. Dealing with the computational complexity of determining the equivariant basis $\mathbf{B}$

Computing  $\mathbf{B}$  amounts to finding the nullspace of a large linear system of equations. Finzi et al. [7] proposes a Krylov gradient-based method able to handle both finite and Lie groups' arbitrary representations. While Van der Pol et al. [23] approximates  $\mathbf{B}$  through SVD of a matrix  $\bar{\mathbf{W}} \in \mathbb{R}^{z \times mn}$  ( $z \geq mn$ ). Both approaches run in polynomial time  $\mathcal{O}(r^2(mn)^2)$  (prohibiting their use in large dimensional spaces) and approximate the space rank  $r$  numerically.

Fortunately, DMS groups  $\mathcal{G}$  are finite having permutation matrices as regular representations (which are used for the internal latent spaces  ${}^l\mathbf{z}$  of the architecture (see fig. 1-right). Such that  $g \cdot \mathbf{z} = \rho_{\mathbf{z}}(g)\mathbf{z} | \mathbf{z} \in \mathcal{Z}, g \in \mathcal{G}$ . Reducing the computation of the nullspace  $\mathbf{B}$  to a search of the unique permutations (or orbits) of  $\mathbf{w}$  in linear time.

To see this, note that the constraints imposed by each  $\rho_{\mathbf{W}}(g)$  result in parameter sharing constraints (e.g.,  $w_{10} = -w_2 = \dots = w_0$ ). In these cases, every vector of the null-space of  $\mathbf{C}$  (i.e.,  $\mathbf{B}_i$ ) simply describes the sharing scheme of a free variable of the system of equations (i.e., the trainable parameter  $c_i$ ), and this sharing scheme is nothing else but one of the unique  $r$  orbits of the dimensions of  $\mathbf{w}$  when transformed by all group actions, e.g.,  $\mathcal{G} \cdot w_{10} = \{g \cdot w_{10} : \forall g \in \mathcal{G}\} = \{w_{10}, -w_2, \dots, w_0\}$  (see the parameter orbits of length 4 in fig. 1-right, for  $\mathcal{K}_4$ ). The orbits of all  $\mathbf{w} \in \mathbf{w}$  are trivially computed with  $[\mathbf{w}, \rho_{\mathbf{W}}(g_1)\mathbf{w}, \dots, \rho_{\mathbf{W}}(g_{|\mathcal{G}|})\mathbf{w}]$ , while the unique  $r$  orbits can be identified in  $\mathcal{O}(mn)$  time. Our proposed solution can be thought of as a linear-time version of Ravanbakhsh et al. [20].

### C. Optimal parameter initialization for equivariant layers

Proper initialization of the equivariant layer's trainable parameters  $c_i$  (eq. (9)) is required to avoid activations/gradients

<sup>7</sup>A similar analysis can be made for the bias vector  $\mathbf{b}$ .

<sup>8</sup> Since in DMSs the input and output groups are isomorphic, a direct product results in an overconstraint of the linear map. Reducing the number of trainable parameters.

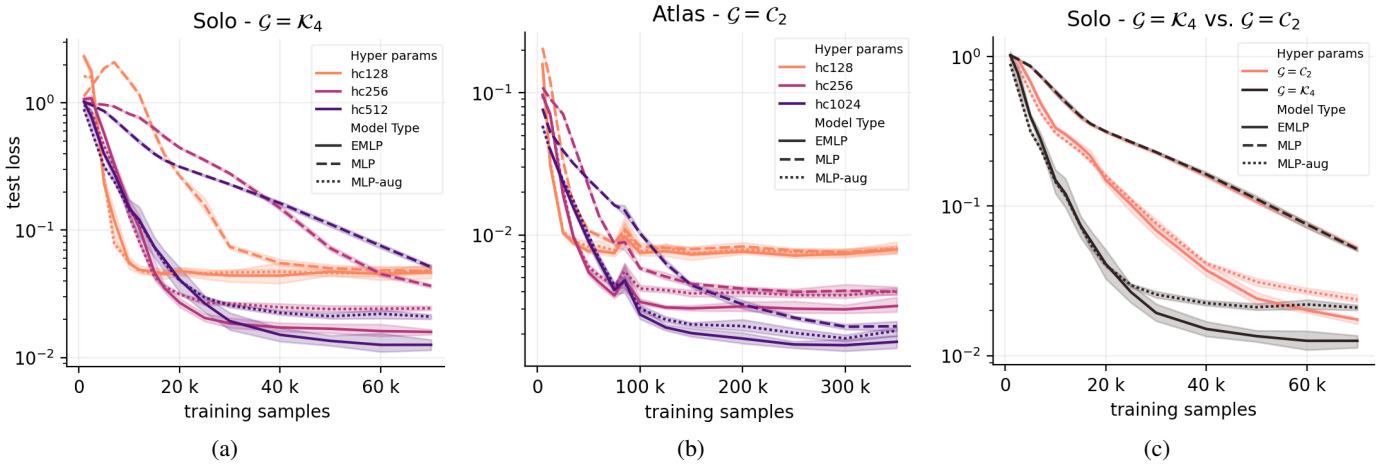


Fig. 3: **CoM-estimation results comparing MLP, MLP-aug, and EMLP models. Left and Middle:** Test set sample efficiency, for robot Solo and Atlas, of model variants with different capacities (number of neurons  $hc$  in hidden layers). **Right:** Sample efficiency for robot Solo (fig. 1), of models with  $hc = 512$ , when exploiting  $\mathcal{G} = \mathcal{K}_4$  (sagittal and traversal symmetries) and  $\mathcal{G} = \mathcal{C}_2 = \{e, g_s\} \subset \mathcal{K}_4$  (only sagittal symmetry). Plots display average and standard deviation across 10 seeds.

from vanishing or exploding [13]. Following the same derivation of the Kaiming initialization [11] (see section B-B), we can conclude that the parameters should be initially sampled from a distribution with  $\text{Var}(c_l) = m/\lambda_{\mathbf{B}}\gamma_{\sigma}$ , to ensure constant variance of activations throughout the network layers (see fig. 7). Where  $\lambda_{\mathbf{B}} = \sum_i^m \sum_j^n \sum_k^r \mathbf{B}_{i,j;k}^2$  and  $\gamma_{\sigma}$  is a nonlinearity dependant scalar (e.g.,  $\gamma_{\text{ReLU}} = 1/2$ ,  $\gamma_{\text{SeLU}} = 1$  following Klambauer et al. [13]). This initialization depends only on  $\mathbf{B}$ . Thus, is applicable to any Lie or finite group.

#### D. Reduction of trainable parameters in equivariant layers:

Determining analytically the number of trainable parameters (i.e. the rank  $r$ ) of an  $\mathcal{G}$ -equivariant layer is, in general, an unresolved problem. However, for DMS groups, we show on section B-A that the number of trainable parameters of a  $\mathcal{G}$ -equivariant layer can range from  $|w|/|\mathcal{G}| \leq r \leq |w|$ , depending on the number of dimensions of the input-output spaces left invariant by the symmetry actions. In practice, this implies that for a  $\mathcal{G}$ -equivariant layer without any input-output fixed points (e.g., all intermediate layers of a  $\mathcal{G}$ -equivariant NN), the number of trainable parameters is reduced by  $1/|\mathcal{G}|$  being  $|\mathcal{G}|$  the group order. Therefore a  $\mathcal{G}$ -equivariant architecture with  $\mathcal{G} = \mathcal{C}_2$  (or  $\mathcal{G} = \mathcal{K}_4$ ) will have approximately  $1/2$  (or  $1/4$ ) of the trainable parameters of an unconstrained NN of the same architectural size (this applies to NN processing data from robot Atlas and Solo fig. 1). The reduction of parameters is caused by the parameter sharing constraints (eq. (9)) and is visually depicted in fig. 1-right.

## VI. EXPERIMENTS

We present two experiments of supervised learning, a regression application using synthetic data and a classification application using real-world data. Both experiments aim to illustrate the versatility of DMSs for data augmentation and training of equivariant functions, along with the impact on the model's sample efficiency and generalization capacity when

exploiting DMSs. While we keep the presentation concise, all the technical aspects are detailed in section C and <sup>1</sup>.

#### A. CoM momentum estimation (Regression)

In this experiment, we train a NN to approximate a robot's center-of-mass momentum given the joint-space position and velocities:  $\mathbf{h} = \mathbf{A}_{\mathcal{G}}(\dot{\mathbf{q}})\dot{\mathbf{q}}$ , where  $\mathbf{h} = [\mathbf{l}^T \mathbf{k}^T]^T$  are the linear  $\mathbf{l}$  and angular  $\mathbf{k}$  momentum components and  $\mathbf{A}_{\mathcal{G}}$  is the Centroidal Momentum Matrix (CMM) of Orin et al. [17]. This analytical function is highly non-linear and  $\mathcal{G}$ -equivariant to the robot's DMS group  $\mathcal{G}$  (eqs. (18) and (20)). Consequently, the function approximator is expected to be equivariant or approximately equivariant.

We test two robots: (1) Atlas, a  $n_J = 30$ [DoF] humanoid robot with a reflection DMS group  $\mathcal{G} = \mathcal{C}_2$  (fig. 1-left). (2) Solo, a  $n_J = 12$ [DoF] quadruped robot with the Klein-4 group as DMS group  $\mathcal{G} = \mathcal{K}_4$  (fig. 1-center). Furthermore, we compare three variants of a function approximation: a standard Multi-Layer Perceptron (MLP), a version of the MLP trained using data augmentation (MLP-aug), and a version of the MLP with hard-equivariance constraints (E-MLP).

On fig. 3-left-&-middle, we compare the model variants. For both robots and all model capacities, the E-MLP and MLP-Aug outperform MLP on sample efficiency (better generalization with fewer data) and robustness to overfitting when training data is scarce. Comparing the E-MLP and MLP-Aug model variants, we see that the lower capacity versions behave similarly, but as capacity increases, E-MLP starts to show better sample efficiency and generalization. Lastly, on (fig. 3-right) we compare, for the robot Solo, the performance of the model variants when exploiting the robots' entire symmetry group ( $\mathcal{K}_4$ ) and a subgroup of the real symmetry group ( $\mathcal{C}_2 \subset \mathcal{K}_4$ ). The results indicate that sample efficiency and generalization capacity increase with the number of **true** symmetries of the data exploited.

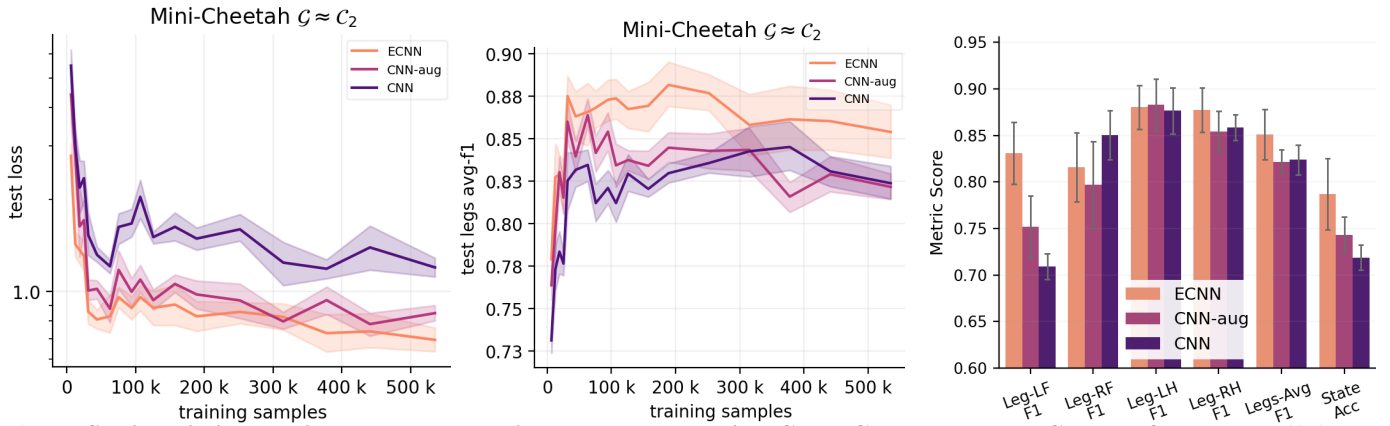


Fig. 4: **Static-Friction-Regime contact detection results comparing CNN, CNN-aug, and ECNN.** **Left:** Sample efficiency in log-log scale. **Middle:** Average legs F1-score **Right:** Classification metrics on test set performance of models trained with the entire training set. Selected metrics are contact-state ( $\mathbf{y} \in \mathbb{R}^{16}$ ) accuracy (Acc) and f1-score (F1) for each leg binary contact state. Due to the sagittal symmetry of the robot, the left front (LF) and right front (RF) legs are expected to be symmetric, as the left hind (LH) and right hind (RH) legs. F1-score is presented considering the dataset class imbalance (see section C-D). Reported values represent the average and standard deviation across 8 different seeds.

### B. Static-friction-regime contact detection (Classification)

This experiment uses the dataset presented in Lin et al. [15] for the estimation of static-friction-regime contacts in each of the four legs of the Mini-Cheetah quadruped robot. These real-world datasets consist of  $\mathbf{x} \in \mathbb{R}^{54 \times 150}$ , the history of the past 150 time-frames of proprioceptive data ( $\hat{\mathbf{q}}, \dot{\hat{\mathbf{q}}}$ , base linear acceleration, base angular velocity, and each of the four legs feet’s position and velocities). Data was obtained from inboard sensors during locomotion, with various gaits and terrains. Along with  $\mathbf{y} \in \mathbb{R}^{16}$ , the ground truth contact state of the robot, estimated off-line using a non-causal algorithm (i.e., dependant on the past and future). The objective is to train a causal function approximator  $f(\mathbf{x}; \phi)$  for the contact state.

The real-world Mini-Cheetah robot has an [approximate](#) reflection DMS  $\mathcal{G} \approx C_2$ . Hence, both the proprioceptive data  $\mathbf{x}$  and the contact state  $\mathbf{y}$  share the symmetry group  $\mathcal{G}$  (see section C-D). We compare three variants of function approximators: the original Conv-NN architecture of Lin et al. [15] (CNN), a version of CNN trained using data-augmentation (CNN-aug), and a version of CNN with hard-equivariance constraints (E-CNN).

The sampling efficiency of the model variants and the average legs contact state classification are illustrated in fig. 4-left-&-middle. Where the equivariant model E-CNN presents better generalization, performance, and robustness to dataset biases (section C-D2) than the unconstrained models across all training set sizes, followed by CNN-aug. In fig. 4-right we evaluate test set classification metrics when using the entire training data. The E-CNN model outperforms both CNN-aug and CNN on contact state classification and average leg contact detection. Of relevant importance is the mitigation of sub-optimal asymmetries of the models by exploiting symmetries. Preventing the model from favoring the classification of one leg above others (see legs LF and RF in fig. 4-right). Refer to section C-E for details.

## VII. CONCLUSIONS & DISCUSSION

In this work, we present the definition of Discrete Morphological Symmetry (DMS). A capability of some dynamical systems to imitate the effect of rotations, translations, and infeasible reflections of space with a feasible discrete change in the system configuration. Using the language of group theory we study the set of DMSs of a dynamical system as a symmetry group  $\mathcal{G}$  and conclude that: (1) A system with a symmetry group  $\mathcal{G}$  has  $\mathcal{G}$ -equivariant generalized mass matrix and  $\mathcal{G}$ -equivariant dynamics. (2) That the symmetries of the dynamics translate to symmetries in optimal control policies and to any proprioceptive and exteroceptive measurements, related to the evolution of the system’s dynamics. Thus, justifying the study of DMSs for their potential for data augmentation and machine learning applications exploiting symmetries.

Furthermore, we present the theoretical abstractions required to study DMSs in arbitrary dynamical systems with any number of symmetries. With this formalism, we identify the reflection/sagittal symmetry of humans (and most animals/robots) as the simplest DMS group  $\mathcal{G} = C_2$ . Additionally, we present several examples of more complex DMS groups involving real robotic systems (for which DMSs can be exploited, but currently are not).

On the practical side, we release an open-access repository enabling the rapid prototyping of  $\mathcal{G}$ -equivariant neural networks for the exploitation of DMS in applications processing data from rigid-body dynamics (e.g., robotics, computer graphics, and computational biology). This repository holds an expanding library of symmetric robotic systems with their groups already identified. Moreover, we present empirical and theoretical results justifying the exploitation of DMSs in data-driven applications through data augmentation or the use of  $\mathcal{G}$ -equivariant NN. Both symmetry exploitation methods result in improved sample efficiency and generalization.



*Limitations:* Our work makes two assumptions: (1) that the system symmetry group  $\mathcal{G}$  is finite, and (2) that the symmetries of the system are exact. For a detailed account of limitations see section D.

*Further work:* For data-driven applications the benefits of DMSs suggest the computational design of symmetrical dynamical systems. While for control applications, the  $\mathcal{G}$ -equivariance nature of the generalized mass matrix suggests research on the numerical implications of this previously unexploited constraint in optimal control.

#### ACKNOWLEDGMENTS

This work’s experiments were run at the Barcelona Supercomputing Center in collaboration with the HPAI group. This work is supported by the Spanish government with the project MoHuCo PID2020-120049RB-I00 and the ERA-Net Chistera project IPALM PCI2019-103386.

#### REFERENCES

- [1] Farzad Abdolhosseini, Hung Yu Ling, Zhaoming Xie, Xue Bin Peng, and Michiel Van de Panne. On learning symmetric locomotion. In *Motion, Interaction and Games*, pages 1–10. 2019.
- [2] Michael M Bronstein, Joan Bruna, Yann LeCun, Arthur Szlam, and Pierre Vandergheynst. Geometric deep learning: going beyond euclidean data. *IEEE Signal Processing Magazine*, 34(4):18–42, 2017.
- [3] Michael M Bronstein, Joan Bruna, Taco Cohen, and Petar Veličković. Geometric deep learning: Grids, groups, graphs, geodesics, and gauges. *arXiv preprint arXiv:2104.13478*, 2021.
- [4] Justin Carpentier, Guilhem Saurel, Gabriele Buondonno, Joseph Mirabel, Florent Lamiroux, Olivier Stasse, and Nicolas Mansard. The pinocchio c++ library: A fast and flexible implementation of rigid body dynamics algorithms and their analytical derivatives. In *2019 IEEE/SICE International Symposium on System Integration (SII)*, pages 614–619. IEEE, 2019.
- [5] Nathan Carter. *Visual group theory*, volume 32. American Mathematical Soc., 2021.
- [6] Marc Finzi, Gregory Benton, and Andrew G Wilson. Residual pathway priors for soft equivariance constraints. *Advances in Neural Information Processing Systems*, 34: 30037–30049, 2021.
- [7] Marc Finzi, Max Welling, and Andrew Gordon Wilson. A practical method for constructing equivariant multilayer perceptrons for arbitrary matrix groups. In *International Conference on Machine Learning*, pages 3318–3328. PMLR, 2021.
- [8] Niklas Funk, Charles Schaff, Rishabh Madan, Takuma Yoneda, Julen Uraín De Jesus, Joe Watson, Ethan K Gordon, Felix Widmaier, Stefan Bauer, Siddhartha S Srinivasa, et al. Benchmarking structured policies and policy optimization for real-world dexterous object manipulation. *IEEE Robotics and Automation Letters*, 7(1): 478–485, 2021.
- [9] Xavier Glorot and Yoshua Bengio. Understanding the difficulty of training deep feedforward neural networks. In *Proceedings of the thirteenth international conference on artificial intelligence and statistics*, pages 249–256. JMLR Workshop and Conference Proceedings, 2010.
- [10] Kaveh Akbari Hamed and Jessy W Grizzle. Event-based stabilization of periodic orbits for underactuated 3-d bipedal robots with left-right symmetry. *IEEE Transactions on Robotics*, 30(2):365–381, 2013.
- [11] Kaiming He, Xiangyu Zhang, Shaoqing Ren, and Jian Sun. Delving deep into rectifiers: Surpassing human-level performance on imagenet classification. In *Proceedings of the IEEE international conference on computer vision*, pages 1026–1034, 2015.
- [12] Gábor Holló. Demystification of animal symmetry: Symmetry is a response to mechanical forces. *Biology Direct*, 12(1):1–18, 2017.
- [13] Günter Klambauer, Thomas Unterthiner, Andreas Mayr, and Sepp Hochreiter. Self-normalizing neural networks. *Advances in neural information processing systems*, 30, 2017.
- [14] Cornelius Lanczos. *The variational principles of mechanics*. University of Toronto press, 2020.
- [15] Tzu-Yuan Lin, Ray Zhang, Justin Yu, and Maani Ghafari. Legged robot state estimation using invariant kalman filtering and learned contact events. In *5th Annual Conference on Robot Learning*, 2021.
- [16] Daniel Ordonez-Apaez, Antonio Agudo, Francesc Moreno-Noguer, and Mario Martin. An adaptable approach to learn realistic legged locomotion without examples. In *2022 International Conference on Robotics and Automation (ICRA)*, pages 4671–4678. IEEE, 2022.
- [17] David E Orin, Ambarish Goswami, and Sung-Hee Lee. Centroidal dynamics of a humanoid robot. *Autonomous robots*, 35(2):161–176, 2013.
- [18] Jim Ostrowski and Joel Burdick. Geometric perspectives on the mechanics and control of robotic locomotion. In *Robotics Research*, pages 536–547. Springer, 1996.
- [19] Robert J Quigley. Pseudovectors and reflections. *American Journal of Physics*, 41(3):428–430, 1973.
- [20] Siamak Ravanbakhsh, Jeff Schneider, and Barnabas Poczos. Equivariance through parameter-sharing. In *International conference on machine learning*, pages 2892–2901. PMLR, 2017.
- [21] Jon M Selig. *Geometric fundamentals of robotics*, volume 128. Springer, 2005.
- [22] Alex Simpkins. System identification: Theory for the user, (Ijung, I.; 1999)[on the shelf]. *IEEE Robotics & Automation Magazine*, 19(2):95–96, 2012.
- [23] Elise Van der Pol, Daniel Worrall, Herke van Hoof, Frans Oliehoek, and Max Welling. Mdp homomorphic networks: Group symmetries in reinforcement learning. *Advances in Neural Information Processing Systems*, 33: 4199–4210, 2020.
- [24] Rui Wang, Robin Walters, and Rose Yu. Approximately equivariant networks for imperfectly symmetric dynam-

ics. *arXiv preprint arXiv:2201.11969*, 2022.

- [25] James T. Wheeler. General coordinate covariance of the euler lagrange equations. Classical Mechanics class notes, 2014. URL <http://www.physics.usu.edu/Wheeler/ClassicalMechanics/CMCoordinateinvarianceofEulerLagrange.pdf>.
- [26] P-B Wieber. Holonomy and nonholonomy in the dynamics of articulated motion. In *Fast motions in biomechanics and robotics*, pages 411–425. Springer, 2006.
- [27] Raymond Yeh, Yuan-Ting Hu, and Alexander Schwing. Chirality nets for human pose regression. *Advances in Neural Information Processing Systems*, 32, 2019.
- [28] Wenhao Yu, Greg Turk, and C Karen Liu. Learning symmetric and low-energy locomotion. *ACM Transactions on Graphics (TOG)*, 37(4):1–12, 2018.
- [29] Martin Zinkevich and Tucker Balch. Symmetry in markov decision processes and its implications for single agent and multi agent learning. In *In Proceedings of the 18th International Conference on Machine Learning*. Citeseer, 2001.

## APPENDIX A

### PROPERTIES OF ROBOTIC SYSTEMS WITH DMSS

Here, we present a geometric (instead of algebraic) development analog to section IV-B. For clarity of the explanation, let us imagine two different Euclidean spaces and two versions of the robot: the original space (with reference frame  $o$ ) and robot with coordinates  $\mathbf{q}$  and  $\dot{\mathbf{q}}$ , and the virtual rotated/reflected space (with a reference frame  $\bar{o}$ , with configuration  ${}^o\mathbf{X}_{\bar{o}} = \begin{bmatrix} \mathbf{R}_{\bar{g}} & \mathbf{r}_{\bar{o}} \\ \mathbf{0} & 1 \end{bmatrix}$ ) and virtual robot with coordinates  $\bar{\mathbf{g}} \cdot \mathbf{q}$  and  $\bar{\mathbf{g}} \cdot \dot{\mathbf{q}}$  referenced to  $\bar{o}$ . Noting that in the case of a reflection, the virtual robot has reflected versions of each rigid body.

For eqs. (3) and (5) to hold, there must exist an action  $g \in \mathcal{G}$  transforming the real robot configuration  $g \cdot \mathbf{q}, g \cdot \dot{\mathbf{q}}$  resulting in the same kinetic energy as the virtual robot’s kinetic energy:

$$\begin{aligned} \mathcal{T}(g \cdot \mathbf{q}, g \cdot \dot{\mathbf{q}}) &= \frac{1}{2} \sum_{i=1}^{n_B} m_i \dot{\mathbf{r}}_{g,i}^T \dot{\mathbf{r}}_{g,i} + \mathbf{w}_{g,i}^T \mathbf{I}_i \mathbf{w}_{g,i} \\ &\doteq \frac{1}{2} \sum_{k=1}^{n_B} \bar{m}_k \dot{\bar{\mathbf{r}}}_k^T \dot{\bar{\mathbf{r}}}_k + \bar{\mathbf{w}}_k^T \bar{\mathbf{I}}_k \bar{\mathbf{w}}_k = \mathcal{T}(\bar{\mathbf{g}} \cdot \mathbf{q}, \bar{\mathbf{g}} \cdot \dot{\mathbf{q}}), \end{aligned} \quad (10)$$

where  $\dot{\mathbf{r}}_{g,i}$ ,  $\mathbf{w}_{g,i}$ ,  $m_i$  and  $\mathbf{I}_i$  are the linear and angular velocity, mass, and inertia matrix of the transformed body  $i$  (referenced to  $o$ ). Likewise,  $\dot{\bar{\mathbf{r}}}_k$ ,  $\bar{\mathbf{w}}_k$ ,  $\bar{m}_k$  and  $\bar{\mathbf{I}}_k$  are the equivalent quantities for the virtual robot and body  $k$  (referenced to  $\bar{o}$ ).

#### A. Symmetries of kinematic parameters:

Ignore momentarily the influence of the mass and inertia in terms of the real and virtual bodies. We can assert that for eq. (10) to hold, the transformed configuration should result in a kinematic tree indistinguishable from the virtual robot’s. Thus, for everybody  $i$  in the real robot kinematic tree, there should exist an equivalent virtual body  $k$  (as seen in fig. 6, not always  $k = i$ ). By equating the linear and angular velocities of the real and virtual bodies, referenced to  $o$ , and expressing the velocities as functions of the generalized coordinates we obtain:

$$\begin{aligned} \dot{\mathbf{r}}_{g,i} &= \dot{\bar{\mathbf{r}}}_k \doteq \mathbf{R}_{\bar{g}} \cdot \dot{\bar{\mathbf{r}}}_k \\ \mathbf{J}_{T_i}(g \cdot \mathbf{q}) g \cdot \dot{\mathbf{q}} &= \mathbf{R}_{\bar{g}} \cdot \mathbf{J}_{T_k}(\mathbf{q}) \dot{\mathbf{q}} \\ \mathbf{J}_{T_i}(g \cdot \mathbf{q}) g &= \mathbf{R}_{\bar{g}} \cdot \mathbf{J}_{T_k}(\mathbf{q}) \end{aligned} \quad (11)$$

$$\begin{aligned} \mathbf{w}_{g,i} &= \bar{\mathbf{w}}_k \doteq |\mathbf{R}_{\bar{g}}| \mathbf{R}_{\bar{g}} \cdot \mathbf{w}_k \\ \mathbf{J}_{R_i}(g \cdot \mathbf{q}) g \cdot \dot{\mathbf{q}} &= |\mathbf{R}_{\bar{g}}| \mathbf{R}_{\bar{g}} \cdot \mathbf{J}_{R_k}(\mathbf{q}) \dot{\mathbf{q}}, \\ \mathbf{J}_{R_i}(g \cdot \mathbf{q}) g &= |\mathbf{R}_{\bar{g}}| \mathbf{R}_{\bar{g}} \cdot \mathbf{J}_{R_k}(\mathbf{q}), \end{aligned} \quad (12)$$

where  $\mathbf{J}_{T_i}(\mathbf{q})$ ,  $\mathbf{J}_{R_i}(\mathbf{q}) \in \mathbb{R}^{3 \times n}$  are the position and orientation analytical Jacobians (describing the instantaneous velocity vectors contributed by each DoF to body  $i$ ) of the real robot at a configuration  $\mathbf{q}$  [26]. Formulating eq. (12) for each of the  $n_B$  bodies of the robot we obtain at best  $n_B \times 3 \times n$  non-linear equations that can be used to assert if  $g$  exists. In practice, the action representation  $\rho_Q(g)$  and especially its component acting on the joint space  $\rho_{Q_J}(g)$  can be trivially determined by solving eq. (12) (or equivalently eq. (7)) for each body from top to bottom of the kinematic tree (i.e., base first, end-effectors last), if  $g$  exists.

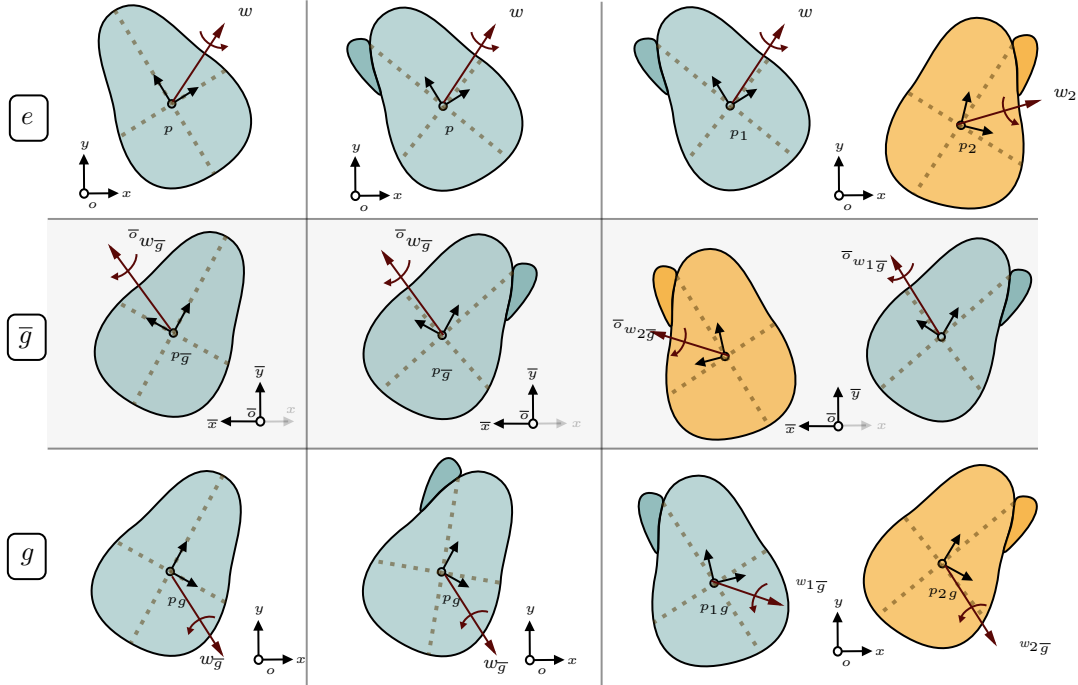


Fig. 5: Properties of bodies capable of imitating a true reflection  $\bar{g}$  of space (w.r.t the  $yz$ -plane in this case), with a proper transformation  $g$  involving only a rotation and translation. The first row shows the original bodies with their respective angular velocities  $w$ , subjected to trivial symmetry transformation  $e$  (dashed lines represent the principle axes of inertia of the bodies), and the second and third rows display the effect of  $\bar{g}$  and  $g$  on the bodies and angular velocities, respectively. The first column displays a rigid body with symmetric mass distribution, for which  $g$  exists, as the reflected and rotated bodies share an equivalent angular kinetic energy. The second column shows a rigid body with asymmetrical mass distribution, for which the rotation  $g$ , that produces a kinematic symmetry, results in the reflected and rotated bodies having different angular kinetic energies (eq. (2)). The third column shows two bodies with asymmetrical mass distributions, each a reflected version of the other, in this case, the action  $g$  swaps bodies configurations to imitate the configuration and energy state of the reflected bodies transformed with  $\bar{g}$ . Angular velocity is a pseudo-vector (or axial-vector), for which a reflection transformation is computed as  $w_{\bar{g}} = |\mathbf{R}_{\bar{g}}| \mathbf{R}_{\bar{g}} w$  (see Quigley [19]).

### B. Symmetries of dynamic parameters

Let us assume kinematic symmetry and direct our attention now to the influence of the mass and inertia terms on the kinetic energy of a single rigid body when it is transformed with the action  $g$ , which imitates a true reflection of space  $\bar{g}$ . Focus on the first two columns of fig. 5. Because of the kinematic symmetry the CoM of the reflected and transformed bodies coincide, both bodies have equivalent linear components of kinetic energy. However, for arbitrary rigid bodies, the reflected and transform bodies will have different angular components of kinetic energy. Note that in the general case, the transformed and reflected bodies' inertia will differ, thus even if both bodies have the same angular velocities, their kinetic energy will differ.

Let  $p$ ,  $p_{\bar{g}}$  and  $p_g$  be frames located at the CoM of the original, reflected and transformed bodies, aligned with the principal axes of inertia of each of the bodies. Similarly, denote  ${}^o\mathbf{I}$  and  ${}^o\mathbf{I}_g$  as the original and transformed bodies inertias referenced to  $o$ , and  ${}^{\bar{o}}\mathbf{I}_{\bar{g}}$  as the reflected body inertia referenced to the reflected Euclidean space  $\bar{o}$ . In order to

comply with eq. (12), we must ensure that:

$$\begin{aligned}
 {}^o w_{\bar{g}}^T {}^o \mathbf{I}_g {}^o w_{\bar{g}} &= {}^{\bar{o}} w_{\bar{g}}^T {}^{\bar{o}} \mathbf{I}_{\bar{g}} {}^{\bar{o}} w_{\bar{g}}, \\
 (\mathbf{R}_{\bar{g}} {}^o w)^T {}^o \mathbf{I}_g (\mathbf{R}_{\bar{g}} {}^o w) &= {}^{\bar{o}} w_{\bar{g}}^T {}^{\bar{o}} \mathbf{I}_{\bar{g}} {}^{\bar{o}} w_{\bar{g}} \\
 |{}^o w_{\bar{g}}| &= |\mathbf{R}_{\bar{g}}| |\mathbf{R}_{\bar{g}} {}^o w|, \\
 {}^o \mathbf{I}_g &= \mathbf{R}_{\bar{g}} {}^{\bar{o}} \mathbf{I}_{\bar{g}} \mathbf{R}_{\bar{g}} \\
 |{}^o w| &\equiv |{}^{\bar{o}} w_{\bar{g}}|, \quad \mathbf{R}_{\bar{g}} \mathbf{R}_{\bar{g}} = \mathbf{I}, \\
 {}^o \mathbf{R}^{p_g p_g} \mathbf{I}_g {}^o \mathbf{R}^{p_g \top} &= \mathbf{R}_{\bar{g}} {}^{\bar{o}} \mathbf{R}^{p_{\bar{g}} p_{\bar{g}}} {}^{\bar{o}} \mathbf{I}_{\bar{g}} {}^{\bar{o}} \mathbf{R}^{p_{\bar{g}} \top} \mathbf{R}_{\bar{g}} \\
 |{}^a \mathbf{I}| &= {}^b \mathbf{R}^{a b} {}^b \mathbf{I} {}^b \mathbf{R}^{a \top}, \\
 {}^o \mathbf{R}^{p_g p_g} \mathbf{I}_g {}^o \mathbf{R}^{p_g \top} &= \mathbf{R}_{\bar{g}} {}^o \mathbf{R}^{p p} \mathbf{R}^{p_{\bar{g}} p_{\bar{g}}} {}^{\bar{o}} \mathbf{I}_{\bar{g}} {}^{\bar{o}} \mathbf{R}^{p_{\bar{g}} \top} \mathbf{R}_{\bar{g}}, \\
 {}^o \mathbf{R}^{p_g} &\doteq \mathbf{R}_{\bar{g}} {}^o \mathbf{R}^{p p} \mathbf{R}^{p_{\bar{g}}} \\
 |{}^p \mathbf{I}| &\equiv {}^p \mathbf{I}_g \equiv {}^p \mathbf{I}_{\bar{g}}.
 \end{aligned} \tag{13a}$$

What eq. (13a) states is that in order for the reflected and transformed bodies to have equivalent angular kinetic energy, both bodies should have co-linear (or aligned) principal axes of inertia. This allows us to describe  ${}^o \mathbf{R}^{p_g}$  as a function of the original body configuration  ${}^o \mathbf{R}^p$  and two reflection matrices: the true reflection of space  $\mathbf{R}_{\bar{g}}$  and a body specific diagonal reflection matrix  ${}^p \mathbf{R}^{p_{\bar{g}}}$ , which exists only if the rigid

body has a symmetric mass distribution. A visual example for symmetric and asymmetrical rigid bodies is presented in fig. 5 left and middle columns. A similar analysis follows for DMSs imitating rotations

### C. Symmetric position and velocity constraint configuration spaces

Although it is implicitly implied on eq. (2) that the constrained position  $Q$  and velocity  $T_q Q$  configuration vector spaces should also be symmetric or equivariant, this property might be easily overlooked. As mentioned in section IV the relevance of morphological symmetries relies on the equivariant nature of the system dynamics (eqs. (1) and (3)), which imprints symmetry constraints on optimal control policies and proprioceptive and exteroceptive measurements. However, with non-symmetric constrained configuration spaces, eq. (2) will not hold for every system state  $q \in Q$ ,  $\dot{q} \in T_q Q$ , and any uncontrolled or controlled trajectory of the system dynamics shall not have a symmetric equivalent trajectory, as this has the potential to violate the constraints of the configuration space.

## APPENDIX B

### EFFICIENT CONSTRUCTION OF $\mathcal{G}$ -EQUIVARIANT NNs FOR DMS GROUPS $\mathcal{G}$

As mentioned in section V our work builds upon the framework for the construction of  $\mathcal{G}$ -equivariant NN of Finzi et al. [7]. The core limitation of this framework is the inability to handle large dimensional spaces, due to the computational and memory complexities. For instance, for an equivariant layer with input dimension  $n$  and output dimension  $m$ , the computational complexity of finding the equivariant linear map basis  $\mathbf{B}$  (which is quadratic  $\mathcal{O}((mn)^2 r^2)$  through the Krylov subspace method) and the memory complexity of  $\mathbf{B} \in \mathbb{R}^{mn \times r} \mid r \leq mn$ , become easily intractable for moderate  $n$  and  $m$  dimensions. This limitation is openly discussed in the EMLP repository *README.md*, but regretfully not in the original paper.

In practice, we found these limitations when trying to construct the equivariant version of the Contact CNN [15] in our second experiment. This architecture in its internal layers has  $n, m > 2000$ , for which: (i) the Krylov subspace method complexity renders the operation intractable with standard hardware and (ii) the matrices  $\mathbf{B}$  of internal layers required storage of  $1[Gb] >$  for moderate input output dimensions ( $m, n \approx 250$ ) and  $1[Pb] >$  for  $m, n > 2000$ ). See section C for a comparison between dense and sparse matrix representations.

#### A. Trainable parameter reduction of $\mathcal{G}$ -equivariant layers (for $\mathcal{G}$ a DMS group)

Determining analytically the number of trainable parameters (i.e. the rank  $r$ ) of an  $\mathcal{G}$ -equivariant layer is, in general, an unresolved problem. However, for DMS groups,  $r$  can be computed once the input-output action representations are known. The requirement to compute  $r$  is that actions affecting the linear maps are a semi-direct product<sup>8</sup> of the input-output groups, and the input-output representations are generalized

permutation matrices. These conditions are met for most DMS groups (see section D).

The equivariance constraints of eq. (9) on linear maps of perceptron (or convolutional) layers imply a reduction of trainable parameters from  $|w| = mn$  to  $|c| = r \leq mn$ . For DMS groups,  $r$  is associated with the number of unique orbits of the elements of  $w$ . Thus we can compute this value using the orbit-counting theorem (also known as Burnside's Lemma), which states that the number of orbits is the average number of fix-points of  $\mathcal{G}$ , that is  $r = \frac{1}{|\mathcal{G}|} \sum_{g \in \mathcal{G}} |w^g|$ , where  $w^g \doteq \{w \in w : g \cdot w = w\}$  represents the set of elements of  $w$  that are invariant to  $g$  (i.e. fix-points). Those fix-points can be identified by the elements on the diagonal of  $\rho_w(g)$  that are equal to one. Therefore, for a  $\mathcal{G}$ -equivariant layer, the number of trainable parameters is determined by:

$$r = \frac{1}{|\mathcal{G}|} \sum_{g \in \mathcal{G}} \chi_{\rho_w}^1(g) = \frac{1}{|\mathcal{G}|} \sum_{g \in \mathcal{G}} \chi_{\rho_{in}}^1(g^{-1}) \cdot \chi_{\rho_{out}}^1(g), \quad (14)$$

denoting  $\chi_{\rho}^1(g) : \mathcal{G} \rightarrow \mathbb{N}$  as the number of fix-points of the action representation  $\rho(g)$ . Therefore, the number of trainable parameters can range from  $|w|/|\mathcal{G}| \leq r \leq |w|$ , depending on the fix-points of the layers' input and output spaces.

#### B. Parameter initialization of equivariant layers for DMS

Consider a Equivariant Neural Network architecture composed of multiple layers of equivariant linear (or convolutional) layers of the form  ${}^l y := \sigma({}^l W {}^l x + {}^l b)$ , being  $l$  the layer index,  ${}^l x \in \mathbb{R}^n$  and  ${}^l y \in \mathbb{R}^m$  the layer's input and output vector spaces,  ${}^l W \doteq \sum_k {}^l c_k {}^l B_{:,k} \in \mathbb{R}^{m \times n}$  the layer's linear map,  ${}^l B \in \mathbb{R}^{m \times n \times r}$  the layer's  $r$  basis vectors spawning the space of equivariant linear maps,  ${}^l c \in \mathbb{R}^r$  the layer's trainable parameters, and  ${}^l b \in \mathbb{R}^m$  the layer's bias vector.

For the optimal flow of information throughout the network, it's relevant to initialize the trainable parameters such that the variance of activations (during inference/forward-propagation) and gradients (during back-propagation) is kept constant, avoiding activations/gradients from vanishing or exploiting [9]<sup>9</sup>.

The derivation is based on the equivalent process for unconstrained layers presented in He et al. [11]. Let the layer's activations before the non-linearity be denoted by  ${}^l z = {}^l W {}^l x + {}^l b$ , such that  ${}^l y = \sigma({}^l z)$ , and note that  ${}^l x = {}^{l-1} y$ . Furthermore, we will assume the elements of  ${}^l c$  and  ${}^l x$  are mutually independent and sampled from two independent distributions, denoting the random variables of the two distributions as  ${}^l c$  and  ${}^l x$ .

The core difference in the initialization of unconstrained and equivariant layers lies in the way the linear map is

<sup>9</sup>See Pierre Ouannes blog: [pouannes.github.io/blog/initialization](https://pouannes.github.io/blog/initialization)



parameterized. For equivariant layers we have:

$$\begin{aligned}
\text{Var}({}^l\mathbf{W}^l\mathbf{x} + {}^l\mathbf{b}) &= \sum_i^m \sum_j^n \text{Var}({}^lW_{i,j} {}^lx_j) \mid \text{Var}({}^l\mathbf{b}) = 0 \\
&= \sum_i^m \sum_j^n \text{Var}\left(\left(\sum_k^r {}^lc_k {}^l\mathbf{B}_{m,n,k}\right) {}^lx_j\right) \\
&= \text{Var}({}^lc {}^lx) \underbrace{\sum_i^m \sum_j^n \sum_k^r \mathbf{B}_{m,n,k}^2}_{\lambda_{\mathbf{B}}} \quad (15) \\
&\mid \text{Var}\left(\sum_a \underbrace{s_a}_{\text{const}} \mathbf{p}\right) = \sum_a s_a^2 \text{Var}(\mathbf{p})
\end{aligned}$$

In the forward-propagation scenario, we are interested in conserving the variance of the activations throughout layers, that is we must ensure  $\text{Var}({}^l\mathbf{z}) = \text{Var}({}^{l-1}\mathbf{z})$ . Using eq. (15) we obtain:

$$\begin{aligned}
\text{Var}({}^l\mathbf{z}) &= \text{Var}({}^l\mathbf{W}^l\mathbf{x} + {}^l\mathbf{b}) \\
m \text{Var}({}^l\mathbf{z}) &= \lambda_{\mathbf{B}} \text{Var}({}^lc {}^lx) \\
\text{Var}({}^l\mathbf{z}) &= \frac{\lambda_{\mathbf{B}}}{m} \left( \underbrace{\mathbb{E}({}^lc^2)}_{\text{Var}({}^lc)} \mathbb{E}({}^lx^2) - \underbrace{\mathbb{E}({}^lc)^2}_{=0} \mathbb{E}({}^lx)^2 \right) \\
\text{Var}({}^l\mathbf{z}) &= \frac{\lambda_{\mathbf{B}}}{m} \text{Var}({}^lc) \mathbb{E}({}^{l-1}\mathbf{y}^2) \\
&\mid {}^lx = {}^{l-1}\mathbf{y} = \sigma({}^{l-1}\mathbf{z}) \\
\text{Var}({}^l\mathbf{z}) &= \frac{\lambda_{\mathbf{B}} \lambda_{\sigma}}{m} \text{Var}({}^lc) \text{Var}({}^{l-1}\mathbf{z}) \quad (16) \\
&\mid \mathbb{E}({}^{l-1}\mathbf{y}^2) = \lambda_{\sigma} \text{Var}({}^{l-1}\mathbf{z}) \\
\text{Var}({}^l\mathbf{z}) &\equiv \text{Var}({}^{l-1}\mathbf{z}) \quad (17) \\
&\mid \text{Var}({}^lc) \doteq \frac{m}{\lambda_{\mathbf{B}} \lambda_{\sigma}}
\end{aligned}$$

where  $\lambda_{\sigma}$  in eq. (16) is a non-linearity dependent scalar computed analytically or empirically (see He et al. [11]). In eq. (17) we conclude that if we sample the equivariant layer trainable parameters  ${}^lc$  from a distribution ensuring  $\text{Var}({}^lc) \doteq \frac{m}{\lambda_{\mathbf{B}} \lambda_{\sigma}}$ , the variance of the activations across equivariant layers remain constant. A similar procedure can be applied to the backward propagation case, concluding that in order to maintain a constant variance of the gradients across the network layers we should sample the trainable parameters ensuring  $\text{Var}({}^lc) \doteq \frac{n}{\lambda_{\mathbf{B}} \lambda_{\sigma}}$ . As remarked in He et al. [11] both variance values for the forward and backward propagation cases lead to the proper flow of information in the network. On fig. 7, it can be appreciated that our method achieves equivalent results for equivariant architectures as [11] does for standard linear and convolutional architectures.

## APPENDIX C IMPLEMENTATION DETAILS & CODE

Additional to this section, we provide open-access code with the scripts for reproducing the experiments of this work,

the parameters of the models used for comparison, along with additional interactive examples visualizing morphological symmetries of both robotic systems and data.

### A. Efficient data augmentation

Since any input  $\mathbf{x}$  and output  $\mathbf{y}$  spaces of equivariant architectures have matrix symmetry action representations,  $\rho_{\mathbf{x}}(g)$ ,  $\rho_{\mathbf{y}}(g)$ , it is possible to perform batched data augmentation, reducing the computational complexity of augmenting a batch of  $N_b$  samples from  $N_b$  matrix-vector multiplications to a single matrix-matrix multiplication, preferably performed after data is loaded to GPU for optimal performance.

### B. Hyperparameter tuning

The only hyper-parameter tuned for each model and model variant was the learning rate. For all model variants presented in this work (except the original Contact-CNN model from Lin et al. [15], which we retrained using the same hyperparameters reported by the authors) we ran a grid-search in log-scale among 20 different learning rates. In this scenario, we always used the entire training dataset and optimized w.r.t computed loss in the entire validation partition. The learning rate values used for each model are depicted in section C-D2.

### C. Experiment: CoM Momentum Estimation

The dataset for the CoM estimation experiment was generated using Pinocchio [4], which in turn uses the URDF models of the robots Solo and Atlas, to extract the kinematic and dynamic parameters required to compute the Centroidal Momentum Matrix  $\mathbf{A}_G(\mathbf{q})$  matrix [17], with which computing the CoM momentum reduces to:

$$g \cdot \mathbf{h} = \mathbf{A}_G(g \cdot \hat{\mathbf{q}}) g \cdot \dot{\hat{\mathbf{q}}} \quad \mid \quad \forall g \in \mathcal{G}. \quad (18)$$

$$g \cdot \mathbf{h} \approx f(g \cdot \hat{\mathbf{q}}, g \cdot \dot{\hat{\mathbf{q}}}; \phi) \quad \mid \quad \forall g \in \mathcal{G}. \quad (19)$$

Where eq. (18) expresses the analytical  $\mathcal{G}$ -equivariant function to compute the CoM momentum. While eq. (19) is the approximation of this function by an  $\mathcal{G}$ -equivariant NN, with parameters  $\phi$ .

1) *Determination of the input and output representations*  $\rho_{\mathbf{x}}(g), \rho_{\mathbf{y}}(g) \mid g \in \mathcal{G}$ : Both robots Solo and Atlas evolve in the Euclidean space of 3-dimensions. Therefore their configuration space can be decoupled into  $\mathbf{Q} \doteq \mathbb{E}_3 \times \mathbf{Q}_J$ . After identifying their symmetry groups and their corresponding  $\mathbb{E}_3$  and  $\mathbf{Q}_J$  representations ( $\rho_{\mathbb{E}_3}(g), \rho_{\mathbf{Q}_J}(g) \mid \forall g \in \mathcal{G}$ ), identifying the representations of the input and output spaces of the NN function approximator (eq. (19)) becomes a trivial task considering that:

$$\begin{aligned}
\underbrace{\begin{bmatrix} \rho_{\mathbb{E}_d}(\bar{g}) & \mathbf{0} \\ \mathbf{0} & \rho_{\mathbb{E}_d}(\bar{g}) \end{bmatrix}}_{\rho_{\mathbf{y}}(g)} \underbrace{\begin{bmatrix} \mathbf{l} \\ \mathbf{k} \end{bmatrix}}_{\mathbf{y}} &\approx f\left(\underbrace{\begin{bmatrix} \rho_{\mathbf{Q}_J}(g) & \mathbf{0} \\ \mathbf{0} & \rho_{\mathbf{Q}_J}(g) \end{bmatrix}}_{\rho_{\mathbf{x}}(g)} \underbrace{\begin{bmatrix} \hat{\mathbf{q}} \\ \dot{\hat{\mathbf{q}}} \end{bmatrix}}_{\mathbf{x}}\right) \\
&\mid \quad \forall (g, \bar{g}) \mid g \in \mathcal{G}, \bar{g} \in \mathbb{E}_3 \quad (20)
\end{aligned}$$

Defining  $\mathbf{x} = \begin{bmatrix} \hat{\mathbf{q}} \\ \dot{\hat{\mathbf{q}}} \end{bmatrix} \in \mathbb{R}^{2n_J}$  and  $\mathbf{y} = \mathbf{h} \in \mathbb{R}^{2d} \equiv \mathbb{R}^6$ . Note that by definition any improper transformation applied to a pseudo-vector (e.g. angular velocity/momentum, torques) is computed as  $|\mathbf{R}|\mathbf{R} \cdot \mathbf{k}$ .

| Layer Type | $n$  | $m$  | Dense Memory [Bytes] |              | Sparse Memory [Bytes] |              |
|------------|------|------|----------------------|--------------|-----------------------|--------------|
|            |      |      | $\rho_w(g)$          | $\mathbf{B}$ | $\rho_w(g)$           | $\mathbf{B}$ |
| 1D-Conv    | 54   | 64   | 764.41M              | 191.10M      | 221.18k               | 110.59k      |
| 1D-Conv    | 64   | 64   | 1.07G                | 268.43M      | 262.14k               | 131.07k      |
| 1D-Conv    | 64   | 128  | 4.29G                | 1.07G        | 524.28k               | 262.14k      |
| 1D-Conv    | 128  | 128  | 17.18G               | 4.29G        | 1.04M                 | 524.28k      |
| Percept    | 4736 | 2048 | 6.02P                | 1.50P        | 620.75M               | 310.37M      |
| Percept    | 2048 | 512  | 70.36T               | 17.59T       | 67.10M                | 33.55M       |
| Percept    | 512  | 16   | 4.29G                | 1.07G        | 524.28k               | 262.14k      |

TABLE I: **Comparison of memory complexity of individual layers of the equivariant version of Contact-CNN [15] (ECNN).** This example compares the sparse and dense representations of matrices  $\mathbf{B} \in \mathbb{R}^{mn \times r}$  and the  $|\mathcal{G}|$  group action representations  $\rho_w(g) \in \mathbb{R}^{mn \times mn}$ , for the symmetry group  $\mathcal{G} = \mathcal{C}_2$  of the Mini-Cheetah robot, with  $r = mn/2$  (see eq. (14)). Here,  $n, m$  represents the input and output dimensions of each layer. The dense memory complexity of all action representations increases with the group order  $|\mathcal{G}|$  while the memory complexity for  $\mathbf{B}$  decreases with larger group orders (since  $r \leq mn$  becomes smaller). We assume floating point representations with 32 bits.

| RF | LF | RH | LH | $\mathbf{y}$ | $g \cdot \mathbf{y}$ | LF | RF | LH | RH |
|----|----|----|----|--------------|----------------------|----|----|----|----|
| 0  | 0  | 0  | 0  | 0            | 0                    | 0  | 0  | 0  | 0  |
| 0  | 0  | 0  | 1  | 1            | 2                    | 0  | 0  | 1  | 0  |
| 0  | 0  | 1  | 0  | 2            | 1                    | 0  | 0  | 0  | 1  |
| 0  | 0  | 1  | 1  | 3            | 3                    | 0  | 0  | 1  | 1  |
| 0  | 1  | 0  | 0  | 4            | 8                    | 1  | 0  | 0  | 0  |
| 0  | 1  | 0  | 1  | 5            | 10                   | 1  | 0  | 1  | 0  |
| 0  | 1  | 1  | 0  | 6            | 9                    | 1  | 0  | 0  | 1  |
| 0  | 1  | 1  | 1  | 7            | 11                   | 1  | 0  | 1  | 1  |
| 1  | 0  | 0  | 0  | 8            | 4                    | 0  | 1  | 0  | 0  |
| 1  | 0  | 0  | 1  | 9            | 6                    | 0  | 1  | 1  | 0  |
| 1  | 0  | 1  | 0  | 10           | 5                    | 0  | 1  | 0  | 1  |
| 1  | 0  | 1  | 1  | 11           | 7                    | 0  | 1  | 1  | 1  |
| 1  | 1  | 0  | 0  | 12           | 12                   | 1  | 1  | 0  | 0  |
| 1  | 1  | 0  | 1  | 13           | 14                   | 1  | 1  | 1  | 0  |
| 1  | 1  | 1  | 0  | 14           | 13                   | 1  | 1  | 0  | 1  |
| 1  | 1  | 1  | 1  | 15           | 15                   | 1  | 1  | 1  | 1  |

robot joint-space positions, velocities, base linear acceleration, base angular velocity, and each of the four legs feet's position and velocities, respectively, referenced to the robots base frame  $B$ .

The function approximator to learn is expected to be approximately equivariant to the reflection group  $\mathcal{C}_2$ , considering the sagittal symmetry of the robot morphology. Therefore:

$$g \cdot \mathbf{y} = f(g \cdot \mathbf{x}; \phi) \quad | \quad g \in \mathcal{G} = \mathcal{C}_2 \quad (21)$$

TABLE II: Symmetric contact state for Mini-Cheetah quadruped robot. Considering its morphological symmetry group  $\mathcal{C}_2 = \{e, g\}$ . Each leg binary contact state (LF: Left Front, RF: Right Front, LH: Left Hind, RH: Right Hind) is displayed with its corresponding robot contact state  $\mathbf{y}$ .

2) *Practical details of the dataset generation:* The URDF files of the robots Solo and Atlas are generated using XACRO scripts, which replicate the structure of limbs to their symmetric counterparts, making the dynamics of the robots in simulation exactly  $\mathcal{G}$ -equivariant. However, the algorithm for computing the CoM momentum from Pinocchio is numerically sensitive, resulting in the orbits of the momentum  $\mathcal{G} \cdot \mathbf{h}$  deviating slightly from the theoretical orbits. Therefore to reduce numerical errors and ensure the theoretical equivariance of the data, we replace every target variable by the average of its orbit  $\mathbf{y} = \mathbf{h} \doteq \frac{1}{|\mathcal{G}|} \sum \mathcal{G} \cdot g^{-1}(\mathbf{A}_G(\rho_Q(g)\dot{\mathbf{q}})\rho_Q(g)\dot{\mathbf{q}}) \quad | \quad \forall \quad g \in \mathcal{G}$ .

#### D. Experiment: Static-Friction-Regime Contact Detection

The dataset presented in [15] is composed of output samples  $\mathbf{y} \in \mathbb{R}^{16}$ , where each dimension of  $\mathbf{y}$  represents a logit of a specific contact state, among the 16 different combinations of each of the 4 legs possible binary contact states. The input samples  $\mathbf{y} = \{\mathbf{z}_i\}_{i=0}^{150} \in \mathbb{R}^{54 \times 150}$ , are a history of 150 samples  $\mathbf{z} = [\hat{\mathbf{q}}, \dot{\hat{\mathbf{q}}}, \mathbf{a}, \mathbf{w}, \mathbf{p}, \mathbf{v}] \in \mathbb{R}^{54}$ . Where  $\hat{\mathbf{q}} \in \mathbb{R}^{n_J}$ ,  $\dot{\hat{\mathbf{q}}} \in \mathbb{R}^{n_J}$ ,  $\mathbf{a} \in \mathbb{R}^3$ ,  $\mathbf{w} \in \mathbb{R}^3$ ,  $\mathbf{p} \in \mathbb{R}^{12}$ ,  $\mathbf{v} \in \mathbb{R}^{12}$  are the MIT-Mini-Cheetah

1) *Determination of the input and output representations*  $\rho_x(g), \rho_y(g) \mid g \in \mathcal{G}$ : The MiniCheetah robot evolves in the Euclidean space of 3-dimensions. Therefore its configuration space can be decoupled into  $\mathbf{Q} \doteq \mathbb{E}_3 \times \mathbf{Q}_J$ . After identifying their symmetry groups and their corresponding  $\mathbb{E}_3$  and  $\mathbf{Q}_J$  representations ( $\rho_{\mathbb{E}_3}(g), \rho_{\mathbf{Q}_J}(g) \mid \forall g \in \mathcal{G}$ ), we can identify the representations of the input and output spaces of the NN function approximator (eq. (21)), considering that:

$$\rho_y(g)\mathbf{y} \approx f\left(\underbrace{\begin{bmatrix} \rho_{\mathbf{Q}_J}(g) & 0 & 0 & 0 & 0 & 0 \\ 0 & \rho_{\mathbf{Q}_J}(g) & 0 & 0 & 0 & 0 \\ 0 & 0 & \rho_{\mathbb{E}_3}(\bar{g}) & 0 & 0 & 0 \\ 0 & 0 & 0 & \rho_{\mathbb{E}_3}(\bar{g}) & 0 & 0 \\ 0 & 0 & 0 & 0 & \rho_p(g) & 0 \\ 0 & 0 & 0 & 0 & 0 & \rho_p(g) \end{bmatrix}}_{\rho_x(g)} \underbrace{\begin{bmatrix} \hat{\mathbf{q}} \\ \dot{\hat{\mathbf{q}}} \\ \mathbf{a} \\ \mathbf{w} \\ \mathbf{p} \\ \mathbf{v} \end{bmatrix}}_{\mathbf{x}}\right) \quad | \quad \forall (g, \bar{g}) \mid g \in \mathcal{G}, \bar{g} \in \mathbb{E}_3$$

Where the representation  $\rho_p(g)$  acting on  $\mathbf{p} \in \mathbb{R}^{12}$  and  $\mathbf{v} \in \mathbb{R}^{12}$  is determined understanding that each of the feet positions ( $\mathbf{p}_{RF}, \mathbf{p}_{LF}, \mathbf{p}_{RH}, \mathbf{p}_{LH}$ ) and velocities ( $\mathbf{v}_{RF}, \mathbf{v}_{LF}, \mathbf{v}_{RH}, \mathbf{v}_{LH}$ ) are simply vectors living in  $\mathbb{E}_3$ . Thus, we must apply the euclidean action  $\rho_{\mathbb{E}_3}(\bar{g})$  while at the same time permuting the feets (similar to the permutation of the

| Robot       | Model    | $\mathcal{G}$                     | lr                   | Samples |
|-------------|----------|-----------------------------------|----------------------|---------|
| Solo        | MLP/EMLP | $\mathcal{C}_2$ & $\mathcal{K}_4$ | $2.4 \times 10^{-3}$ | 100k    |
| Atlas       | MLP/EMLP | $\mathcal{C}_2$                   | $1.5 \times 10^{-3}$ | 500k    |
| MiniCheetah | CNN      | $\mathcal{C}_2$                   | $1.0 \times 10^{-4}$ | 730k    |
| MiniCheetah | E-CNN    | $\mathcal{C}_2$                   | $1.0 \times 10^{-5}$ |         |

TABLE III: Robot, Models and Dataset parameters.

kinematic subchains described by  $\rho_{Q_J}(g)$ :

$$g \cdot \mathbf{p} = \underbrace{\rho_{\mathbb{R}^4}(g) \otimes \rho_{\mathbb{E}_3}(\bar{g})}_{\rho_{\mathbf{p}}(g)} \mathbf{p}, \quad |\forall(g, \bar{g})|g \in \mathcal{G}, \bar{g} \in \mathbb{E}_3 \quad (22)$$

$$= \begin{bmatrix} 0 & 1 & 0 & 0 \\ 1 & 0 & 0 & 0 \\ 0 & 0 & 0 & 1 \\ 0 & 0 & 1 & 0 \end{bmatrix} \otimes \rho_{\mathbb{E}_3}(\bar{g}) \begin{bmatrix} \mathbf{p}_{RF} \\ \mathbf{p}_{LF} \\ \mathbf{p}_{RH} \\ \mathbf{p}_{LH} \end{bmatrix} \quad |g \neq e$$

$$g \cdot \mathbf{v} = \underbrace{\rho_{\mathbb{R}^4}(g) \otimes \rho_{\mathbb{E}_3}(\bar{g})}_{\rho_{\mathbf{p}}(g)} \mathbf{v} \quad |\forall(g, \bar{g})|g \in \mathcal{G}, \bar{g} \in \mathbb{E}_3 \quad (23)$$

$$= \begin{bmatrix} 0 & 1 & 0 & 0 \\ 1 & 0 & 0 & 0 \\ 0 & 0 & 0 & 1 \\ 0 & 0 & 1 & 0 \end{bmatrix} \otimes \rho_{\mathbb{E}_3}(\bar{g}) \begin{bmatrix} \mathbf{v}_{RF} \\ \mathbf{v}_{LF} \\ \mathbf{v}_{RH} \\ \mathbf{v}_{LH} \end{bmatrix} \quad |g \neq e$$

Being  $\rho_{\mathbb{R}^4}(g) \mid \forall g \in \mathcal{C}_2$  two regular representations of  $\mathcal{C}_2$  stack in block diagonal form to form a representation in 4-dimensional space, representing the right-left symmetries of the 4 kinematic tree's subchains. The nature of the representation  $\rho_{Q_J}(g) \doteq \rho_{\mathbb{R}^4}(g) \otimes \mathbf{I}_{n_s}$  might be better understood if you consider that we apply  $\rho_{\mathbb{R}^4}(g)$  to the number of degrees of freedom of the kinematic subchain  $n_s$  (which for the case of MiniCheetah is  $n_s = 3$  DoF). See simpler examples in fig. 6.

Lastly, the representation for the contact state  $\rho_{\mathbf{y}}(g)$  is given by the permutation matrix relating  $\mathbf{y}$  and  $g \cdot \mathbf{y}$  described in section C-D.

2) *Details on dataset partitioning:* We modified the original dataset partitioning to properly evaluate the generalization capacity of the models. The original dataset was composed of 15 different recordings varying ground type and gait type used during data collection (most recordings were performed on a trot gait, which heavily biased the dataset to contact states 0, 6, and 9 of section C-D).

The authors of [15] partitioned all 15 recordings into (70%, 15%, 15%) training, validation and testing. This partition was made such that the first 70% time-samples of each recording were assigned for training, the following 15% to validation, and the rest for testing.

Because we are interested in studying the generalization capacity of the models and the out-of-training-distribution performance, we modified this partitioning such that among the 15 different recordings we selected randomly 5 recordings for testing, and the remaining 10 recordings were used for training splitting these recordings into (85%, 15%) training and validation splits as in [15], that is, for each recording, the first 85% data-samples go for training and the remaining for validation.

The selected training-validation recordings were: air walking gait, concrete difficult slippery, concrete left circle, middle pebble, rock road, asphalt road, concrete galloping, grass, old asphalt road, sidewalk. While the selected testing recordings were: air jumping gait, concrete pronking, concrete right circle, forest, small pebble.

## E. Mitigation of suboptimal asymmetries in model performance

When comparing individual leg classification we see that the equivariant model converges to having a similar performance for each symmetric pair of legs, while the unconstrained models converge to an asymmetrical suboptimal state favoring the contact detection of one leg at the expense of reduced performance for the symmetric leg (see LF and RF f1-scores). This asymmetrical performance is attributed to the CNN and CNN-aug models learning to extract temporal features for both symmetric legs separately, increasing the likelihood of converging to asymmetrical local minima. On the contrary, the equivariant model E-CNN can be thought of as learning to extract a single set of *symmetric* temporal features for each symmetric pair of states (a consequence of the model's equivariance and parameter sharing). This implies that the temporal features used for determining the contact state of, say the left frontal leg, would also be used to determine the contact state of the symmetric leg, the right frontal leg, and vice-versa.

## F. Equivariant Conv1D layers

For details on the construction of the Equivariant 1D Convolutional layers refer to <sup>1</sup>. Note that the symmetry of a single time-sample  $\mathbf{z}_i$  is shared across all time-samples  $\mathbf{y} = \{\mathbf{z}_i\}_{i=0}^{150}$ .

## APPENDIX D LIMITATIONS

Our work makes two main assumptions:

- 1) **Symmetries are exact:** By assuming that a dynamical system has exact and not approximate symmetries we are departing from the real-world nature of DMSs since for any robotic system in the real-world the manufacturing and assembly process introduces errors/tolerances in the kinematic and dynamic parameters of each of the robot's bodies. Likewise, the dynamics of animals in nature are not perfectly equivariant since morphological symmetries are only approximate symmetries. Although exact symmetries seem to be a strong assumption, in practice, the reality is that it is a common assumption in the fields of robotics and control theory, in which idealized models of the dynamics are often assumed (in simulation and real-world).

On section VI we show that the exact symmetry bias is justifiable and beneficial for learning function approximators processing the dynamics of approximately symmetrical systems in the real world. However, the authors highlight the necessity to properly address the case of approximate equivariance, which we leave to future work. To address this case, system identification techniques [22] have been wildly used to approximate the deviation of the kinematic and dynamic parameters from the assumed values. While in the case of  $\mathcal{G}$ -equivariant NN Wang et al. [24], Finzi et al. [6] provide

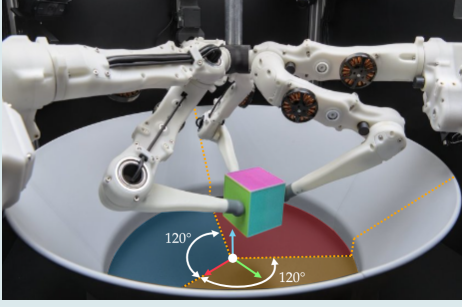
clear and valuable approaches to learn approximate  $\mathcal{G}$ -equivariant NN.

It is relevant to highlight that, in physics-based simulation, the most common practice is to work with the idealized model of dynamics. Thus, the assumption of exact symmetries is justifiable and encouraged in applications where simulation is a relevant tool.

- 2) **Symmetry group is finite:** This work narrows its focus to DMSs, even do the definition of DMS eq. (5) can be relaxed to cover continuous morphological symmetries (an example of this continuous symmetry is the capability of a robot arm manipulator to imitate rotations of space by rotating its first degree of freedom). This assumption allows us to compute in linear time the basis **B** of equivariant linear maps (restricted to groups with finite regular matrix representations).



**Tri-Finger Robot  $\mathcal{G} = \mathcal{C}_3$**



This fixed-based robot is symmetric w.r.t. rotations of space by  $\theta = 120^\circ$  in the vertical axis. Therefore, its symmetry group is the cyclic group of order three ( $\mathcal{G} = \mathcal{C}_3$ ). To identify this symmetry group we apply the procedure in section IV-C: nosep, leftmargin=\*

- 1) **Identify  $X_B$  and  $I_B$ :** As a fix-based robot, we define  $X_B$  to be the mounting structure supporting each finger, and the gray disk delimiting the workspace (see image).
- 2) **Identify symmetries of  $I_B$ :** The inertia of this virtual base  $I_B$  is invariant to rotations by  $120^\circ$  in the vertical axis. I.e.,  $I_B$  is invariant to  $X_B \rho_{\mathbb{E}_3}(\bar{g})^{-1} | \bar{g} \in \{e, \bar{g}_\theta, \bar{g}_\theta^2\} \equiv \mathcal{C}_3$  (eq. (6)).
- 3) **Identify modularity in the kinematic tree:** There are three symmetric kinematic subchains. Each finger is composed of replicated versions of the same bodies.
- 4) **Identify the DMS group  $\mathcal{G}$ :**

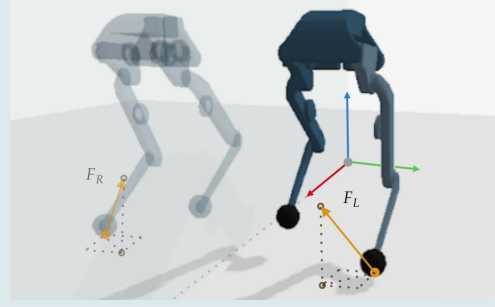
Consider that the transformation  $\rho_{\mathbb{E}_3}(g) X_B \doteq \rho_{\mathbb{E}_3}(\bar{g}) X_B \rho_{\mathbb{E}_3}(\bar{g})^{-1}$  (eq. (6)) can be interpreted as a rotation of the virtual base by  $\theta^\circ$  followed by a rotation  $-\theta^\circ$  in the  $z$  axis. Thus respecting the fix-base constraint of the system. Denote the joint-space  $\mathbf{q} = \hat{\mathbf{q}} = [\mathbf{q}_{f1}^\top, \mathbf{q}_{f2}^\top, \mathbf{q}_{f3}^\top]^\top$  be composed of each finger's DoF ( $\mathbf{q}_{fi} \in \mathbb{R}^3$ ).

Then we can define  $\rho_{\mathbb{Q}_J}(g) \doteq \rho_{\mathbb{R}^3}(\bar{g}) \otimes \mathbf{I}_3 \mid \bar{g} \in \mathcal{C}_3$ . Being  $\rho_{\mathbb{R}^3}(\cdot)$  the permutation representation of 3 elements of  $\mathcal{C}_3$  (3 kinematic subchains). For the generator action of the group this is  $\rho_{\mathbb{R}^3}(\bar{g}) = \begin{bmatrix} 0 & 1 & 0 \\ 0 & 0 & 1 \\ 1 & 0 & 0 \end{bmatrix}$ .

Lastly, we verify if  $\mathcal{G} = \mathcal{C}_3$  by testing all tentative group actions for DMSs eq. (5).

**Augmentation of data samples:** Say we collect a dataset of robot states  $(\mathbf{q}, \dot{\mathbf{q}})$  and cube states  $X_C$  at every time step  $t$ , to train the manipulation policy [8]. To obtain the symmetric states, at every  $t$ , we need to understand that since we are imitating the effect of a true rotation of space  $\bar{g}$ , the symmetric states are obtained by  $(g \cdot \mathbf{q}, g \cdot \dot{\mathbf{q}})$  and  $(\bar{g} \cdot X_C \doteq \rho_{\mathbb{E}_3}(\bar{g}) X_C)$ .

**Bolt Bipedal Robot  $\mathcal{G} = \mathcal{C}_2$**



Bolt is a bipedal robot with a sagittal plane reflection symmetry ( $\mathcal{G} = \mathcal{C}_2$ ). This morphological symmetry allows it to imitate the effect of arbitrary reflections of space ( $\bar{g} \in \mathbb{E}_3$ ) by re-configuring its base and legs. To identify this symmetry group we apply the procedure in section IV-C: nosep, leftmargin=\*

- 1) **Identify  $X_B$  and  $I_B$ :**  $X_B$  is the robot base (hips) body, with its corresponding inertia  $I_B$
- 2) **Identify symmetries of  $I_B$ :** The base body has symmetrical mass distribution w.r.t the sagittal plane. Thus,  $I_B$  is invariant to the transformation  $X_B \rho_{\mathbb{E}_3}(\bar{g})^{-1} | \bar{g} \in \{e, \bar{g}_s\} \equiv \mathcal{C}_2$  (eq. (6)).
- 3) **Identify modularity in the kinematic tree:** There are two symmetric kinematic subchains. The left leg subchain and bodies are reflected versions of the right leg subchain and bodies.
- 4) **Identify the DMS group  $\mathcal{G}$ :**

Since a reflection w.r.t to the sagittal plane would imply a true reflection of the rigid bodies of the legs, we need to *permute* each body in the kinematic tree with each reflected version. Denote the joint-space  $\hat{\mathbf{q}} = [\mathbf{q}_L^\top, \mathbf{q}_R^\top]^\top$  as composed of the left  $L$  and right  $R$  legs' DoF ( $\mathbf{q}_{L/R} \in \mathbb{R}^3$ ). Denote the sign-relation between the DoF of the Left and right legs' degrees of freedom as  $s_{L|R} \in \mathbb{R}^3$ .

Then we can define  $\rho_{\mathbb{Q}_J}(g) \doteq \rho_{\mathbb{R}^2}(\bar{g}) \otimes (s_{L|R} \mathbf{I}_3) \mid \bar{g} \in \mathcal{C}_2$ . Being  $\rho_{\mathbb{R}^2}(\cdot)$  the permutation representation of a 2 elements of  $\mathcal{C}_2$  (2 kinematic subchains). For the non-trivial action of the group this is  $\rho_{\mathbb{R}^2}(\bar{g}_s) = \begin{bmatrix} 0 & 1 \\ 1 & 0 \end{bmatrix}$ .

Lastly, recalling the definition of  $\rho_{\mathbb{E}_3}(g)$  in eq. (6), we verify if  $\mathcal{G} = \mathcal{C}_2$  by testing all tentative group actions for DMSs eq. (5).

**Augmentation of data samples:** Say we collect a dataset of robot states  $(\mathbf{q}, \dot{\mathbf{q}})$  and ground reaction forces  $(\mathbf{f}_L, \mathbf{f}_R)$ , that we transform to the space of generalized forces as  $(\boldsymbol{\tau}_{fL}, \boldsymbol{\tau}_{fR})$ , at every timestep  $t$ . This dataset can be used to train a reactive locomotion policy as in Ordonez-Apaez et al. [16]. The symmetric states, at every  $t$ , are then defined as:  $(g \cdot \mathbf{q}, g \cdot \dot{\mathbf{q}})$  and  $(g \cdot \boldsymbol{\tau}_{fL}, g \cdot \boldsymbol{\tau}_{fR}) \equiv (\rho_{\mathbb{Q}}(g) \boldsymbol{\tau}_{fL}, \rho_{\mathbb{Q}}(g) \boldsymbol{\tau}_{fR})$

Fig. 6: **Tutorial** example morphological symmetries of the Tri-Finger [8] and Bolt robots.

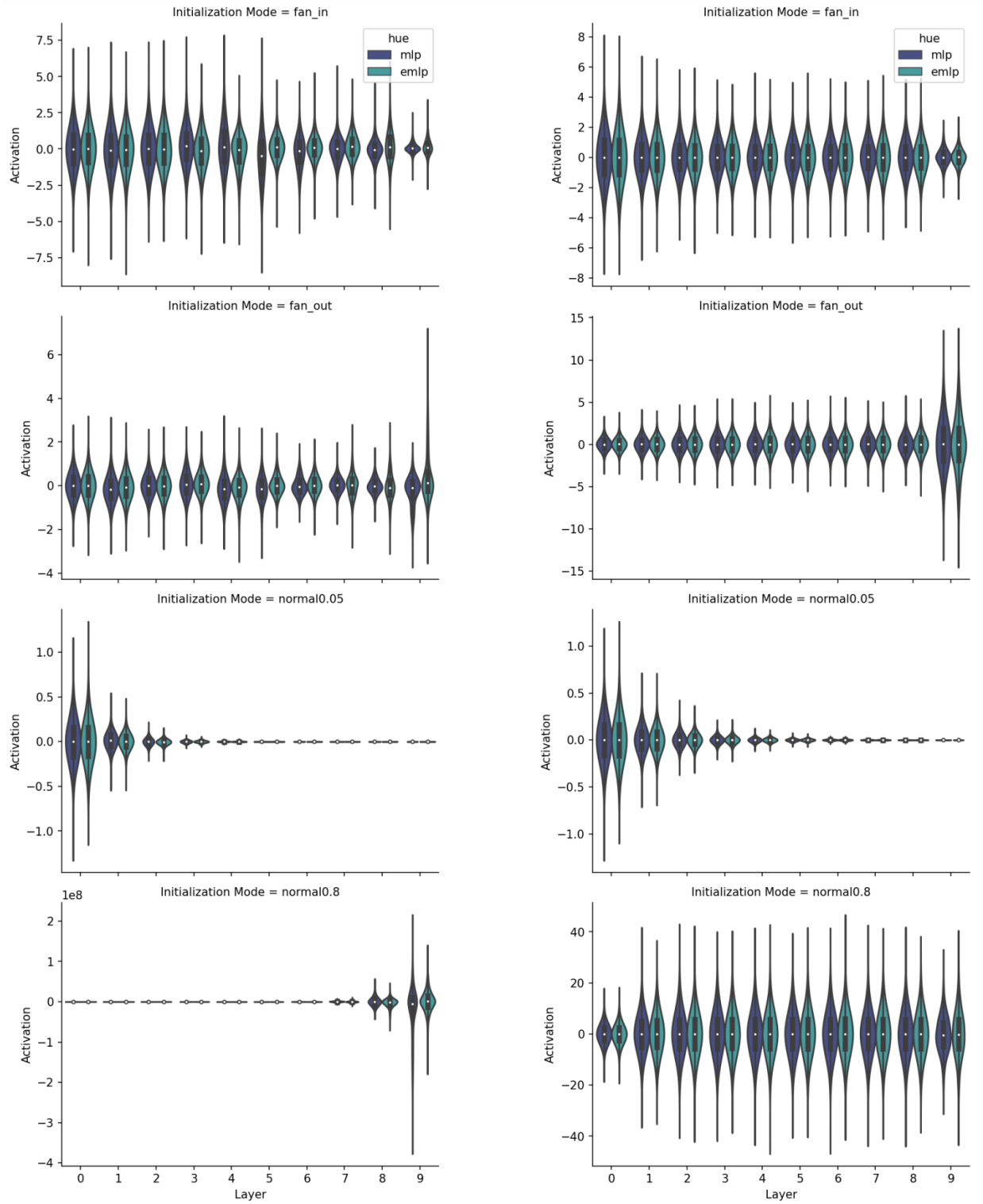


Fig. 7: Comparison of the initialization method of unconstrained layers of He et al. [11] with our initialization method for equivariant layers. Left and right columns correspond to MLP & EMLP architectures with  $\sigma = \text{ReLU}$  (left) and  $\sigma = \text{Tanh}$  (right) non-linearities. Each row shows different initialization methods differing in the variance of the initialization distribution of the layer’s trainable parameters. First and second rows show the forward and backward propagation cases of [11] for MLP and of section B-B for EMLP, with  $\text{Var}^{(l_c)} \doteq m/(\lambda_{l_B} \lambda_\sigma)$  and  $\text{Var}^{(l_c)} \doteq n/(\lambda_{l_B} \lambda_\sigma)$ , respectively. In these cases, the variance of activations through the network depth remains nearly constant, as desired. The last two rows show the initialization of layer parameters with a constant variance of  $0.05^2$  and  $0.8^2$ , illustrating scenarios of activations vanishing and exploding. All intermediate layers have 256 neurons. In the equivariant case, the network is  $\mathcal{K}_4$ -equivariant.